

Flow models of perforated manifolds and plates for the design of a large thermal storage tank for district heating with minimal maldistribution and thermocline growth

M. Pilotelli, B. Grassi, A.M. Lezzi, G.P. Beretta*

Università degli Studi di Brescia, via Branze 38, Brescia, Italy

ARTICLE INFO

Keywords:

Thermal energy storage
District heating
Thermal stratification
Large water tank
Distribution design
Perforated plate

ABSTRACT

Large water tanks are used as thermal energy storage components in district heating systems to store sensible heat produced by intermittent energy sources and to decouple the production of thermal energy from its demand. Good thermal stratification is crucial for energy storage efficiency, thus flow maldistribution and mixing of water layers at different temperatures should be minimized. This paper proposes an innovative internal flow distribution configuration for a large-size thermal energy storage, and develops new simplified analytical models for the choice of its design parameters. In the novel configuration, water is injected into (and collected from) the cap volumes of the tank by flowing radially inward (outward) through several small orifices of a peripheral toroidal manifold. Two horizontal perforated plates cover the full cross sections downstream of the manifolds and rectify the vertical flow, thus reducing mixing. Uniform perforation pitch was analytically demonstrated to be the most reasonable solution both for the toroidal distributors and for the rectifying plates. A 1D model was developed to predict the time evolution of the vertical temperature distribution in the tank. The turbulence-related parameters that could not be inferred from the existing fluid-mechanics literature were initially estimated with CFD simulations. The results of CFD-calibrated model were then compared to experimental data obtained from a full-scale large water-tank facility recently built in Brescia according to the proposed design. After a re-calibration of the exponent defining the decay of homogeneous turbulence downstream of the perforated plates, good agreement was found between measured and predicted vertical temperatures. With the novel inlet design, a thermocline of about 0.5 m is established immediately downstream of the perforated plate, and remains practically constant along time. The model is important to minimize and control the thermocline thickness so as to maximize the recoverable thermal energy, not only at the tank design stage but also to identify optimal loading and unloading protocols.

1. Introduction

District heating systems often use large water tanks as thermal energy buffers to store sensible heat from intermittent energy sources, to cope with peaks of thermal energy demand, to provide some degree of temporal decoupling between the demand of thermal energy and its production, and in some cases also to compensate for water contraction/expansion in the piping network. Typical volumes of thermal storage tanks for industrial and district heating are between 800 and 20000 m³. An extensive review of solar heating systems employing seasonal sensible water storage in artificial large scale basins was proposed in [1].

Although such large thermal reservoirs are important and widespread in Northern European countries [2], the scientific literature on efficient thermal energy storage (TES) is almost entirely devoted to much

smaller water tanks, characterized by volumes between 150 and 2000 liters, typically used for domestic electric boilers and solar hot water systems. An approach to estimate the daily thermal request of buildings in large networks and, consequently, to optimize the operating conditions was presented in [3]. Due to the huge difference in volume, the fluid mechanics and heat transfer phenomenology and, therefore, models and design criteria developed for small water tanks cannot be extrapolated to large tanks. Existing studies on large tanks only investigate their interaction with the district heating demand [4], and the temperature distribution by means of some experimental tests [5]. Other studies focus on the interaction between district heating system and the electricity system [6]: results indicate a clear increase in value of heat generation units in district heating systems that can offer flexibility in a future with increased volatility of electricity prices. To

* Corresponding author.

E-mail address: gianpaolo.beretta@unibs.it (G.P. Beretta).

Nomenclature

Symbols

A	geometrical dimensionless constant [-]
c	specific heat [$\text{kJ kg}^{-1} \text{K}^{-1}$]
C_μ	turbulence model constant [-]
D	tank diameter [m]
d	plate orifice diameter [m]
D_T	manifold centerline diameter [m]
d_T	manifold orifice diameter [m]
D_{TCS}	manifold inner cross-sectional diameter [m]
g	gravitational acceleration [m s^{-2}]
H	tank height [m]
h_0	heat transfer coefficient [$\text{W m}^{-2} \text{K}^{-1}$]
H_{eff}	effective storage height [m]
h_r	height of the water layer above the upper plate/below the lower plate [m]
K	static pressure regain coefficient [-]
k	turbulence kinetic energy [$\text{m}^2 \text{s}^{-2}$]
L	merging distance from perforated plate [m]
\bar{L}	dimensionless merging distance from the perforated plate [-]
L_T	length of the toroidal manifold [m]
n	decay homogeneous turbulent exponent [-]
P_0	pressure at the section of the <i>vena contracta</i> of the perforated plates orifice [Pa]
$P_{0, [\text{inj}/\text{suc}]}$	static pressure in the manifold in injection (“inj”) or suction (“suc”) mode [Pa]
P_∞	pressure far downstream of the perforated plates orifice [Pa]
P_a	pressure downstream of the manifold orifice [Pa]
P_{atm}	atmospheric pressure [Pa]
P_d	pressure below the upper plate/above the lower plate [Pa]
P_R	pressure downstream of the manifold orifices where the jets have merged [Pa]
P_r	pressure immediately above the upper plate/below the lower plate at coordinate r [Pa]
P_s	pressure in the manifold at position s [Pa]
p_{sat}	saturation pressure [Pa]
Pr	Prandtl number [-]
Pr_{turb}	turbulent Prandtl number [-]

Q	water flow rate [kg s^{-1}]
Q_0	water flow rate at the inlet section of each branch of the toroidal manifold [kg s^{-1}]
q''	heat flux [W m^{-2}]
R	tank radius [m]
R_{TCS}	manifold inner cross-sectional radius [m]
Re	Reynolds number [-]
Re_{turb}	turbulent Reynolds number [-]
Re_{Vd}	Reynolds number based on the plate orifice diameter d and the velocity at the <i>vena contracta</i> V [-]
Re_{wz}	Reynolds number based on plate perforation pitch z and vertical mean velocity w [-]
s	position along the toroidal manifold [m]
\bar{s}	dimensionless position along the toroidal manifold [-]
T	temperature [K] or [$^{\circ}\text{C}$]
t	thickness [m]
T_0	temperature of the inflow through the plate orifices [K] or [$^{\circ}\text{C}$]
T_H	hot water temperature [K] or [$^{\circ}\text{C}$]
T_L	cold water temperature [K] or [$^{\circ}\text{C}$]
T_m	mean water temperature [K] or [$^{\circ}\text{C}$]
$U_{0, [\text{inj}/\text{suc}]}$	mean axial velocity at the inlet section in injection (“inj”) or suction (“suc”) mode [m s^{-1}]
U_R	radial velocity in the tank [m s^{-1}]
U_r	radial velocity immediately above the upper plate/below the lower plate at coordinate r [m s^{-1}]
U_s	mean axial velocity near the manifold orifice at position s [m s^{-1}]
V	velocity at the <i>vena contracta</i> [m s^{-1}]
V_0	velocity at the <i>vena contracta</i> in correspondence of manifold inlet in injection mode [m s^{-1}]
V_s	velocity at the <i>vena contracta</i> in correspondence of manifold position s [m s^{-1}]
w	vertical velocity [m s^{-1}]
w_r	volume flow rate per unit of plate area at radial coordinate r [$\text{m}^3 \text{s}^{-1} \text{m}^{-2}$]
x	vertical distance from perforated plate [m]
\bar{x}	dimensionless vertical distance from the perforated plate [-]
x_0	virtual origin of the jet [m]
z	orifice pitch of the perforated plate [m]
z_s	orifice pitch of the toroidal manifold [m]

investigate the effects of differences between design and actual load and, consequently, define an optimal operation strategy, a model was designed by [7].

To fill the literature gap, this paper develops analytical models and design criteria to predict and control maldistribution and thermal stratification. These models and criteria are necessary in order to maximize energy storage efficiency and optimize the daily operation of large water tanks. The phenomenological considerations and the proposed model equations provided in this paper refer to two key internal components: a toroidal perforated pipe distributor and a perforated plate rectifier. To fix ideas and illustrate the results that can be obtained with this model, an innovative design based on the use of both such components is studied. This design has been adopted by the Italian utility A2A for a series of high-efficiency thermal storage tanks that

the company is building in the Brescia, Bergamo, and Milano district heating systems.

Thermal stratification (TS) in water tanks is the result of a complex interplay of fluid mechanics and heat transfer phenomena. As a result, TS depends on many variables, among which the inlet/outlet distributor position and geometry, the presence of obstacles/diffusers in their vicinity, and the thermal mixing produced by forced and natural convection. Inlet/outlet distributors and obstacles should be designed so as to minimize the mixing of water at different temperatures. To maintain stable TS, cold water must flow in and out at the bottom of the tank, and hot water at the top. However, perfect TS is practically

Acronyms

CHP	Combined heat and power
RKE	Realizable $k - \epsilon$
SSTKW	Shear stress transport $k - \omega$
TES	Thermal energy storage
TS	Thermal stratification
WTE	Waste-to-energy

Greek symbols

α	thermal diffusivity [$\text{m}^2 \text{s}^{-1}$]
α_{eff}	effective thermal diffusivity [$\text{m}^2 \text{s}^{-1}$]
α_{turb}	turbulent thermal diffusivity [$\text{m}^2 \text{s}^{-1}$]
β	volumetric thermal expansion [K^{-1}]
ϵ_{eff}	dimensionless effective thermal diffusivity [-]
ϵ	turbulence dissipation rate [$\text{m}^2 \text{s}^{-3}$]
η	maldistribution coefficient [-]
Θ	dimensionless temperature [-]
λ	thermal conductivity [$\text{W m}^{-1} \text{K}^{-1}$]
ν	kinematic viscosity [$\text{m}^2 \text{s}^{-1}$]
ρ	density [kg m^{-3}]
σ	fluid dynamic solidity ratio [-]
τ	time [s], [min] or [h]
$\bar{\tau}$	dimensionless time [-]
ϕ	discharge coefficient [-]

Subscripts

s	position along manifold length
d	below the upper plate/above the lower plate
eff	effective
H	hot water volume
i	insulating layer
inj	injection mode
L	cold water volume
plate	perforated plate
s	steel
suc	suction mode
T	toroidal manifold
TCS	toroidal manifold (cross section)
turb	turbulent

impossible, because even in the most quiescent state of the tank, thermal diffusion and wall boundary layers driven by natural convection contribute to increase the thickness of the *thermocline*, namely, the horizontal layer that separates the lower cold mass from the upper hot mass. Being at intermediate temperatures, the energy stored in the thermocline layer is unusable. Therefore, water tank design and management aiming at high thermal storage efficiency should focus on minimizing the thickness of the thermocline, for example by reducing velocity and pressure disuniformities, and convective mixing, and by adopting optimal charging/discharging protocols. Hence, the need to understand the phenomenology in play and to have simplified models that can be used to predict and control the growth of the thermocline.

In the literature on small water tanks, numerous studies have investigated these aspects. Numerical experiments show that the main parameters affecting TS are the Reynolds number [8] and the shape of the diffuser [8–10]. For example, [8] focused on the diffuser configuration in rectangular tanks, and it was found that the Reynolds number and the diffuser shape are the most affecting parameters.

Altuntop et al. [9] investigated the effects of obstacle placed in the tank to improve TS, and different obstacle configurations were analyzed: a better stratification was found for obstacles with a gap at the center. Zachar et al. [10] investigated the influence of a plate positioned opposite to the inlet, and showed that the diameter of the plate affects the temperature distribution: to preserve the TS, the plate diameter must be at least 75% of the tank diameter. According to [11], the diffuser should be placed as close as possible to the bottom of the tank. The importance of turbulent mixing caused by different inlet configurations was emphasized in [12–14] whose model for thermocline formation showed the key role played by the turbulent diffusivity and its law of decay downstream of the distributor. With the exception of few works, like the recent one by Kocijel et al. [15], most of the studies available in the literature on short-term storage systems provide model and parameters that can help in the design of small domestic and solar water tanks, but they do not scale up to large tanks, except qualitatively. Hence, the need for specific studies to fill the knowledge gap on several important details. In particular, the present study shows that experimental data and numerical analyses available in the literature on flows past perforated manifolds and perforated plates do not cover the range of parameters of interest to the present application, calling for further experimental and numerical studies.

The present article proposes an innovative inlet distributor to reduce flow maldistribution and improve thermal stratification in large TES tanks of district heating networks. The system consists of two components: a toroidal perforated pipe distributor and a perforated plate rectifier. The new configuration is characterized by high-velocity radial injection from the tank wall inwards; therefore, it is based on the opposite concept with respect to standard diffusers usually adopted in district heating storages, where water enters the tank in a central point and flows outwards at low velocity. The study addresses the essential fluid dynamic and heat transfer phenomenology that determines the performance of the two key components. The objective of the analytical and modeling considerations provided is to minimize the effects of velocity non-uniformities, turbulent mixing, and effective thermal diffusivity in the storage section of the tank, between the lower and upper perforated plates, so as to minimize and control the growth of the thermocline thickness and hence maximize the recoverable thermal energy. To this end, a one-dimensional model that predicts the vertical temperature evolution in time is developed and validated. The model parameters for which no analytical, empirical or experimental reference in the literature is available yet are first estimated with numerical simulations, and then verified and adjusted based on field temperature and flow rate measurements.

The paper is structured as follows. Section 2 describes the proposed design configuration and the field of application. Sections 3 and 4 address the problem of maldistribution related to orifice pitch for the toroidal distributors and the rectifying plates, respectively. Section 5 discusses the development of turbulence and flow uniformity downstream of the orifices of the perforated plate, and develops a 1D model for the time evolution of the vertical temperature distribution in the water tank. Section 6 describes the numerical results obtained from the proposed 1D formulation. Section 7 presents a first experimental validation of the model. Conclusions and indications for future work needed to fill the literature gap are drawn in Section 8. Appendices provide mathematical details about the derivation of maldistribution degrees in toroidal distributors and of the free surface shape.

2. Nominal physical dimensions and operating conditions

The system chosen to exemplify the design study is a large storage tank integrated in the Brescia (Italy) district heating network, that has over 25000 m^3 of circulating water in more than 600 km of double pipes (Fig. 1). Most of the heat is produced in a waste-to-energy (WTE) plant, a gas-fired boiler plant, and a combined heat and power (CHP) plant. Recently, waste heat recovery from two steel factories has also

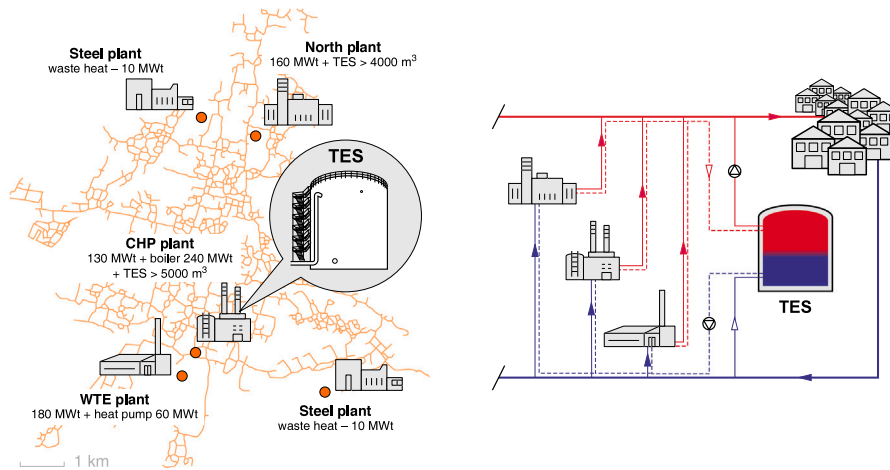


Fig. 1. Left: position of the considered TES in the Brescia district heating network. Right: conceptual schematic layout of the TES charge and discharge modes.

been integrated in the network. During cold winter nights, water at $T_H = 98^\circ\text{C}$ is fed into the tank from the top, while $T_L = 60^\circ\text{C}$ water is extracted from the bottom and returned to the production facilities. During early-morning peak-heat-demand hours, the stored hot water is pumped out of the tank from the top and mixed with the water heated by the production plants and recovered from industrial processes into the district-heating feed pipelines, while the 60°C water from the district-heating return pipelines is fed into the tank from the bottom.

External height and diameter of the storage tank are both 20 m. The internal design configuration chosen for the considered high-efficiency large district-heating water tank design is sketched in Fig. 2. It is characterized by an upper and a lower peripheral toroidal perforated distributor manifold, and an upper and a lower flow-rectifying perforated plate. The internal diameter is $D = 19.5$ m, and the actual height of the storage section (between the upper and lower perforated plates) is $H = 15.7$ m, because about 1000 m³ of volume above the upper plate are used to gain additional flexibility in the management of thermal expansion and water losses. Assuming the thermocline height is less than 1 m, the effective storage height is at least $H_{\text{eff}} = 14.7$ m.

The wall is made of two layers: the inner structural layer made of steel (S275JR, $\rho_s = 7800$ kg/m³, $\lambda_s = 45$ W/mK, $c_s = 470$ J/kg K) of thickness $t_s = 8$ mm (bottom) to 5 mm (top) covered by an external insulating layer made of mineral wool ($\rho_i = 120$ kg/m³, $\lambda_i = 0.039$ W/mK, $c_i = 1030$ J/kg K) of thickness $t_i = 200$ mm.

The upper and lower perforated toroidal manifolds have nominal inner cross-sectional diameter $D_{\text{TCS}} = 500$ mm and centerline diameter $D_T = 18.4$ m. Based on the analyses illustrated in Sections 3 and 4, the toroids have uniform perforation pitch $z_T = 200$ mm with orifices of diameter $d_T = 30$ mm, and the upper and lower perforated plates have uniform square pattern perforation pitch $z = 60$ mm and orifice diameter $d = 5$ mm.

The nominal water flow rate is $Q = 1500$ m³/h, so that the vertical mean velocity is $w = 1.395$ mm/s. Considering water properties at the average temperature of 80°C ($\rho = 975$ kg/m³, $\lambda = 0.67$ W/mK, $c = 4.197$ kJ/kg K, $\beta = 6.521 \times 10^{-4}$ K⁻¹, $\nu = 3.90 \times 10^{-7}$ m²/s), the thermal capacity of the storage tank is $(T_H - T_L) \frac{1}{4} \pi D^2 H_{\text{eff}} \rho c = 200$ MWh, which means that it can deliver a thermal power of $(T_H - T_L) \rho c Q = 68.2$ MW for a little less than three hours (or, on the other hand, that it can be fully charged in almost three hours at that power).

3. Minimizing maldistribution from the toroidal manifolds

Water is charged and discharged from the tank by means of two toroidal tubes installed along the perimeter at the top and at the bottom of the tank. As stated in the Introduction, previous studies

demonstrated that installing the inlet/outlet ports at the extremities of the tank facilitates TS [14]. The function of the toroidal manifold is to guarantee a uniform horizontal radial velocity of the water, inward at inlet and outward at outlet, so as to limit water mixing as much as possible.

A sketch of a section of the toroidal manifold is illustrated in Fig. 3 showing the orifices facing the axis of the tank, drilled horizontally and orthogonally to it. The distance from the toroidal manifold inlet section, measured along its centerline, is denoted by s and reaches the maximum value L_T at the section diametrically opposite to the inlet section. If the toroid, attached as close as possible to the inner wall of the tank, has centerline diameter D_T , then $L_T = \pi D_T$. The mean axial velocity of the water near the orifice at position s is denoted by U_s . The orifices have diameter d_T and are drilled at a pitch z_s which for the purposes of the analysis is assumed to be a function of s , although the present study will show that it can be chosen constant for simplicity of construction without causing significant maldistribution. The mean water velocity at the *vena contracta* of the jet through the orifice at position s is denoted by V_s .

Injection mode

At the tube inlet ($s = 0$) the overall volume flow rate Q into the water tank splits into the two identical branches of the toroidal distributor. In each branch the flow rate at the inlet section is $Q_0 = Q/2 = \pi R_{\text{TCS}}^2 U_{0,\text{inj}}$, being $R_{\text{TCS}} = D_{\text{TCS}}/2$, whereas at the generic position s it is $Q_s = \pi R_{\text{TCS}}^2 U_s$. The pressure inside the manifold is P_s . Ideally, to avoid perimetral maldistribution, a variable pitch z_s of the orifices should be chosen so that the flow rate Q_s decreases linearly with s from Q_0 at $s = 0$, where the static pressure inside the manifold is $P_{0,\text{inj}}$, to 0 at $s = L_T$, where the pressure is P_{L_T} . Therefore, the ideal axial flow rate and velocity in the toroid are $Q_s = (1 - s/L_T) Q_0$ and $U_s = (1 - s/L_T) U_{0,\text{inj}}$, respectively. The assumed linear dependence on s is supported by the more detailed analysis of the problem of maldistribution in a perforated manifold given in Appendix A.

Neglecting viscous effects inside the toroid, the Bernoulli equation applied to an axial streamline between 0 and s , $P_s + \frac{1}{2} \rho U_s^2 = P_{0,\text{inj}} + \frac{1}{2} \rho U_{0,\text{inj}}^2$, yields

$$P_s = P_{0,\text{inj}} + \frac{\rho U_{0,\text{inj}}^2}{L_T} s \left(1 - \frac{s}{2L_T} \right) \quad (1)$$

In particular, at the stagnation point in the toroid, at the $s = L_T$ section diametrically opposite to the inlet section, the static pressure is $P_{L_T} = P_{0,\text{inj}} + \frac{1}{2} \rho U_{0,\text{inj}}^2$.

The flow rate through the orifice at s is $\Delta Q_s = (\pi d_T^2/4) \phi V_s$ where $(\pi d_T^2/4) \phi$ is the cross section and V_s the velocity at the *vena contracta*.

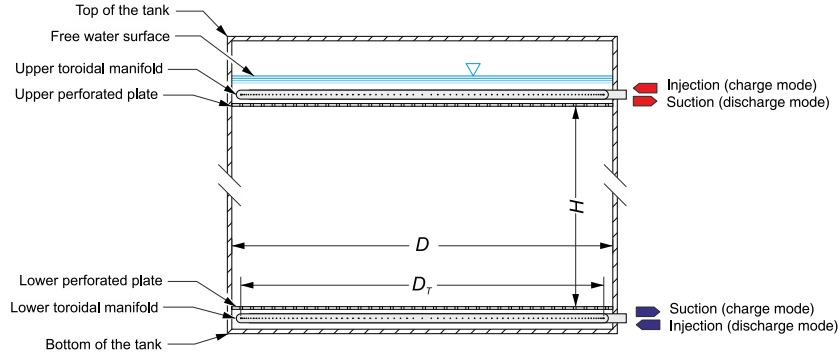


Fig. 2. Schematic geometry of the water tank showing the positions of the upper and lower toroidal manifolds and perforated plates.

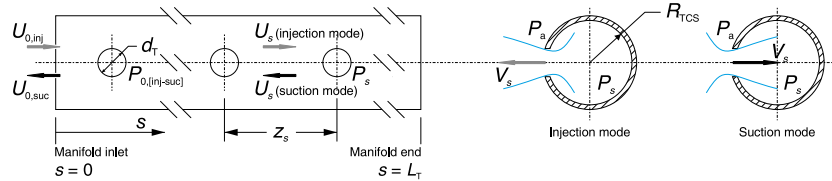


Fig. 3. Sketch of the perforated manifold showing the main flow variables for both the injection (subscript “inj”) and the suction (subscript “suc”) modes.

The next orifice downstream is at distance $s + z_s$ and sees the axial flow rate in the toroid reduced by $\Delta Q_s = (z_s/L_T)Q_0$. Therefore, the velocity at the *vena contracta* is

$$V_s = \frac{4z_s}{\pi d_T^2 \phi} \frac{\Delta Q_s}{z_s} = \frac{4z_s Q_0}{\pi d_T^2 \phi L_T} = \frac{4z_s R_{TCS}^2 U_{0,inj}}{d_T^2 \phi L_T} \quad (2)$$

Pressure drops across single orifices, perforated pipes and perforated plates have been studied widely for a variety of applications both experimentally (see, e.g., [16–21]) and numerically (see, e.g., [22]). Bailey [16] investigated air flow through a single holes in a pipe wall and the coefficient of static pressure regain was determined. Taliyan et al. [17] investigated experimentally the variation of the pressure loss coefficient of pipe perforations with geometrical parameters and Reynolds number. According to [18], the pressure drop across dry perforated plates is affected by the hole diameter, hole pitch, plate thickness, fraction of the plate covered by the perforated area, and a Reynolds number based on the hole diameter, and these results were extended by [19] for a wider Reynolds number range. Flow emerging from perforated plates in relation to the measuring locations and geometry of the perforated plates was investigated experimentally by [20], and the study focused on static pressures, velocity distributions and flow angles at the rear side of the perforated plates. The dependence of the pressure losses through sharp-edged perforated plates with respect to the geometrical and flow parameters was investigated experimentally by [21].

No experimental data are available for a perforated toroidal manifold arrangement but, consistently with the data and analyses in [16] and references therein, the present analysis assumes $\phi = 0.62$ for the discharge coefficient, neglects the effects of the Reynolds number, the pipe thickness, and the pressure recovery in the orifice jet wake, and assumes that the dynamic head of the *vena contracta* is totally dissipated in the mixing downstream (i.e., negligible regain coefficient, $K_{inj} \ll 1$, see Appendix A), so that the static pressure drop across the orifice at position s is

$$P_s - P_a = \frac{1}{2} \rho V_s^2 \quad (3)$$

where P_a is the pressure at some distance downstream of the orifice.

Combining Eqs. (1), (2), and (3), by eliminating the variables P_s and V_s , provides the s dependence of the orifice pitch z_s that guarantees the

condition of vanishing maldistribution

$$z_s = \frac{\phi d_T^2 L_T}{4 R_{TCS}^2} \left[\frac{P_{0,inj} - P_a}{\frac{1}{2} \rho U_{0,inj}^2} + \frac{s}{L_T} \left(2 - \frac{s}{L_T} \right) \right]^{1/2} \quad (4)$$

It is noteworthy that by accepting a sufficiently large static pressure difference $P_{0,inj} - P_a \gg \frac{1}{2} \rho U_{0,inj}^2$ between the inlet of the toroid and the pool in which its orifices discharge, it is possible to make the second term in the square bracket of Eq. (4) (which is bound by 1) negligible with respect to the first, so that the orifice pitch z_s can be chosen uniform, independent of s ,

$$z_s = \frac{\phi d_T^2 L_T}{4 R_{TCS}^2} \left(\frac{P_{0,inj} - P_a}{\frac{1}{2} \rho U_{0,inj}^2} \right)^{1/2} \quad (5)$$

while the resulting maldistribution is small, quantified (see Appendix A) by $(V_T - V_0)/V_T \approx \frac{1}{4} \rho U_{0,inj}^2 / (P_{0,inj} - P_a) \ll 1$, with V_0 and V_T velocities at the *vena contracta* in correspondence of $s = 0$ and $s = L_T$, respectively.

The choice of a uniform perforation pitch is important because the upper and lower toroidal manifolds in the storage tank cycle between the injection and the suction modes. Appendix A shows that whereas the variable-pitch design according to Eq. (4) presents no maldistribution in the injection mode, it does imply maldistribution in the suction mode. Instead, the condition $P_{0,inj} - P_a \gg \frac{1}{2} \rho U_{0,inj}^2$ allows for negligible maldistribution in both modes even with the constructively simpler choice of a uniform perforation pitch.

Suction mode

During the suction mode, the static pressure $P_{0,suc}$ at the outlet section of the toroidal manifold is lower than the pressure P_a in the pool upstream of the orifices. The same assumptions that lead to Eq. (3), including a negligible regain coefficient, $K_{suc} \ll 1$ (see Appendix A) now yield

$$P_a - P_s = \frac{1}{2} \rho V_s^2 \quad (6)$$

where now V_s is the inward velocity at the *vena contracta*. Assuming a given variable-pitch or constant-pitch distribution z_s of the orifices has

been chosen according to either Eq. (4) or Eq. (5), respectively, Eq. (2) is substituted by the continuity equation

$$V_s = -\frac{4z_s}{\pi d_T^2 \phi} \frac{dQ_s}{ds} = -\frac{4z_s R_{TCS}^2}{d_T^2 \phi} \frac{dU_s}{ds} \quad (7)$$

where now U_s is the axial velocity inside the manifold in the direction towards the outlet port, and a continuous model is assumed whereby $\Delta Q_s/z_s = -dQ_s/ds$ (see Appendix A). Here, U_s is not assumed to be linear in s . In fact, the Bernoulli equation applied to the axial streamline between s and 0, $P_s + \frac{1}{2}\rho U_s^2 = P_{0,suc} + \frac{1}{2}\rho U_{0,suc}^2$, combined with Eq. (6), yields

$$P_a - P_{0,suc} = \frac{1}{2}\rho U_{0,suc}^2 - \frac{1}{2}\rho U_s^2 + \frac{1}{2}\rho V_s^2 \quad (8)$$

Therefore, the dependence of U_s is regulated by the differential equation obtained by eliminating V_s from Eqs. (7) and (8),

$$\frac{4z_s R_{TCS}^2}{d_T^2 \phi U_{0,suc}} \frac{dU_s}{ds} = -\left[\frac{P_a - P_{0,suc}}{\frac{1}{2}\rho U_{0,suc}^2} - 1 + \frac{U_s^2}{U_{0,suc}^2} \right]^{1/2} \quad (9)$$

with boundary conditions $U_s(0) = U_{0,suc}$ and $U_s(L_T) = 0$. The equation is solved analytically in Appendix A where relations are also obtained between the perforation pitch distribution $z_s(s)$ and the static pressure difference during the injection mode, $(P_{0,inj} - P_a)/\frac{1}{2}\rho U_{0,inj}^2$, and during the suction mode, $(P_a - P_{0,suc})/\frac{1}{2}\rho U_{0,suc}^2$.

Estimating the pressure difference $P_a - P_{0,suc}$ during the suction mode of the upper manifold is important to avoid cavitation at the outlet port ($s = 0$) where the static pressure reaches its minimum value $P_{0,suc}$. This condition in turn fixes the maximum acceptable temperature in the water tank,

$$P_{0,suc} > p_{sat}(T_{H,max}) \quad (10)$$

4. Minimizing maldistribution from the perforated plates

Previous studies have shown that the presence of a perforated plate reduces the turbulent mixing significantly [12–14]. Therefore, the design proposed in this work includes two perforated plates installed according to Fig. 2. This section develops a simple model of the flow through a perforated plate. The objective is to select the design parameters, in particular, the plate perforation pitch z and the orifice diameter d , so as to minimize the effects of maldistribution and turbulent mixing on the growth of the thermocline. The plate entails a pressure drop due to the entry of the flow into each orifice and the turbulent jet expansion downstream of the *vena contracta* section until the jet wakes merge into a homogeneous turbulent flat front.

For construction simplicity a square perforation pattern is considered, but the results are easily extended to hexagonal and other patterns.

In theory, the flow configurations of the upper and lower plates are different. With reference to Fig. 4, the water layer above the upper plate has a height h_r , which potentially varies with r , and is delimited by a free surface at uniform pressure P_{atm} (atmospheric pressure in this design, but it could be the vapor pressure in a pressurized tank design). On the other hand, the water layer below the lower plate has a fixed height but is instead delimited by the bottom floor of the tank. In principle, therefore, the two perforated plate configurations feature two different maldistribution laws and the condition of vanishing maldistribution would require a nonuniform perforation pitch to orifice diameter ratio. However, it is shown below that for very low vertical water velocity w and a reasonable, not too high, pressure drop across the perforated plates, the maldistribution is negligible even for the simple choice of a uniform perforation pitch.

With reference to Fig. 4, the following notation is introduced: P_r denotes both the pressure immediately above the upper plate and the pressure below the lower plate, near the orifices located at a radial distance between r and $r + dr$ from the tank axis where the horizontal

radial component of the water flow is U_r (inward during injection, outward during suction). P_d denotes the pressure below the upper perforated plate and above the lower perforated plate, at a distance from the plate where the jets have merged into a uniform vertical velocity profile with flow speed w (downward during charge, upward during discharge); V_r denotes the mean flow velocity at the *vena contracta* at radius r , located slightly below the perforated plates during the charge mode and slightly above during discharge; h_r denotes the height of the water layer above the upper plate/below the lower plate (in the latter case constant with radius r). Above the upper plate, $P_r = P_{atm} + \rho gh_r$.

The volume flow rate through the orifice at r is $(\pi d^2/4)\phi V_r$, where $(\pi d^2/4)\phi$ is the cross section of the *vena contracta* and again $\phi = 0.62$. Considering the perforation pitch z_r , the plate area belonging to the orifice is z_r^2 and so the volume flow rate per unit of plate area is $w_r = \pi d^2 \phi V_r / 4z_r^2$. Mass balance requires in general the differential condition

$$d(2\pi r h_r U_r) = 2\pi r w_r dr \quad (11)$$

If, consistently with the present design objective, w_r is assumed uniform, independent of r , i.e., $w_r = w$ ($w = 1.395$ mm/s for nominal conditions), then Eq. (11) integrates to

$$U_r = rw/2h_r \quad (12)$$

where h_r can be assumed constant in all cases, including that of the free surface over the upper plate because in this case the condition $w^2 r^2 / 8gh_r^3 \ll 1$ is always satisfied (for $h_r = 0.5$ m, $w^2 D^2 / 32gh_r^3 = 1.886 \times 10^{-5}$) and, therefore, as shown in Appendix B, the free surface is essentially flat, i.e., $h_r \approx h_c$.

Neglecting viscous effects upstream of the perforated plate, and the small annulus downstream of the orifices of the toroidal manifold where the horizontal jets have not yet merged into a uniform horizontal, radially-directed velocity profile, the Bernoulli equation applied to a radial streamline near the plate between $R = D/2$ and r reads $P_r + \frac{1}{2}\rho U_r^2 = P_R + \frac{1}{2}\rho U_R^2$. This equation, combined with the assumption that the dynamic head of the *vena contracta* is almost entirely dissipated in the mixing downstream so that $P_r - P_d = \pm(1 - K)\frac{1}{2}\rho V_r^2$ (+ for injection, - for suction), where the static pressure regain coefficient $K = \pi d^2 / 4z_r^2 \ll 1$ and is therefore negligible, yields the relation

$$\frac{z_r^4}{d^4} = \pm \frac{\pi^2 \phi^2}{16} \left(\frac{P_R - P_d}{\frac{1}{2}\rho w^2} - \frac{R^2 - r^2}{4h_c^2} \right) \quad (13)$$

This equation determines the r -dependence of the variable perforation pitch z_r needed to satisfy the no-maldistribution (i.e., $w = \text{const}$) condition and shows that, in general, this condition cannot be satisfied for both the injection and the suction mode. However, in this case $\rho w^2 R^2 / 8h_c^2 = 0.09$ Pa so that, for any reasonable choice of the pressure drop across the perforated plates, the second term in the bracket is negligible with respect to the first. Therefore, maldistribution can be avoided with a uniform perforation pitch z , by choosing the z/d ratio according to the relation

$$\frac{z}{d} = \frac{\sqrt{\pi} \phi}{2} \left(\frac{\Delta P_{\text{plate}}}{\frac{1}{2}\rho w^2} \right)^{0.25} \quad (14)$$

provided in the charge and discharge modes a reasonable pressure differences across the plates is accepted,

$$\Delta P_{\text{plate}} = (P_R - P_d)_{\text{inj}} = (P_d - P_R)_{\text{suc}} \quad (15)$$

which in turn determines structural loads on the plates in addition to their own weight. For example, selecting $z = 60$ and $d = 5$ mm and assuming water properties at 80°C (see Section 2), Eq. (14) yields $\Delta P_{\text{plate}} = 83$ Pa, i.e., the pressure generated load on the plate is 8.46 kg/m², while the jet velocity at the *vena contracta* is $V = \sqrt{2\Delta P_{\text{plate}}/\rho} = 0.41$ m/s. Values of these quantities obtained for other diameters are reported in Table 1, together with the Reynolds number based on V and d , $Re_{V,d}$. The Reynolds number based on w and z , $Re_{w,z}$, is 215 and does not depend on the orifice diameter.

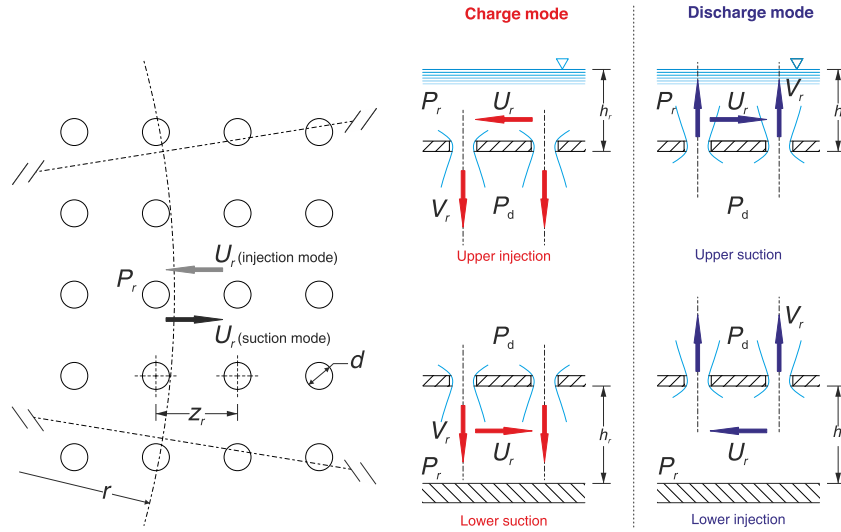


Fig. 4. Sketch of the perforated plates showing the main flow variables for both the charge and discharge modes. In the lower portion of the tank, h_r is constant.

Table 1

Values of pressure- and velocity-related parameters with uniform orifice pitch $z = 60$ mm and three different orifice diameters d .

	$d = 3$ mm	$d = 5$ mm	$d = 10$ mm
ΔP_{plate} [Pa]	640	83	5
V [m/s]	1.15	0.41	0.10
Re_{Vd} [-]	8815	5289	2644

5. Minimizing turbulent thermal mixing downstream of the perforated plates

The jets downstream of a perforated plate eventually merge into a turbulent flow, homogeneous in the horizontal planes, with vertical velocity w . Turbulence intensity decays with the distance x from the plate.

The role of turbulent thermal diffusivity in determining the growth rate of the thermocline in a large thermal tank can be illustrated by means of the well-known analytical solution of the textbook heat transfer problem of two semi-infinite bodies initially at different temperatures, T_H and T_L , which at time $\tau = 0$ are placed in thermal contact at the plane $x_i = x_{0,i}$. Such idealized condition applies to the present TS problem when the complex mixing effects caused by the wall thermal boundary layers and the inlet/outlet maldistribution can be neglected, so that the flow velocity can be assumed uniform everywhere and equal to $\pm w$ (+ for the discharge mode, - for the charge mode). In this highly idealized one-dimensional problem, the initial temperature distribution jumps from T_L to T_H at $x_i = x_{0,i}$, the horizontal thermocline center plane is at $x_i = x_{0,i} \pm w\tau$, and the effective thermal diffusivity $\alpha_{eff} = \alpha + \alpha_{turb}$ (with $\alpha = \lambda/\rho c$) is independent of temperature and position. The heat conduction equation (see, e.g., [23]) has the S-shaped analytical solution

$$T = \frac{T_H + T_L}{2} + \frac{T_H - T_L}{2} \operatorname{erf} \left[\frac{x_i - (x_{0,i} \pm w\tau)}{2\sqrt{\alpha_{eff}\tau}} \right] \quad (16)$$

Defining the thermocline thickness $t_{\delta T}$ as the distance between the x_i where the temperature is $T_L + \delta T$ and the x_i where it is $T_H - \delta T$ for some small preset δT , this solution yields

$$t_{\delta T}(\tau) = 4 \operatorname{erfcinv} \left[\frac{2\delta T}{T_H - T_L} \right] \sqrt{\alpha_{eff}\tau} \quad (17)$$

where $\operatorname{erfcinv}$ denotes the inverse of the error function (also denoted by erfc^{-1}). For the temperature range of interest, $T_L = 60^\circ\text{C}$, $T_H = 98^\circ\text{C}$, the thermal diffusivity changes by 5.7%, $\alpha_L = 0.159$ mm²/s, $\alpha_H =$

0.168 mm²/s. However, it is important to realize that, due to turbulence, α_{eff} may be two or even three orders of magnitude higher than α . So, for example, choosing $\delta T = 1^\circ\text{C}$ and using the value $\alpha = 0.164$ mm²/s, the thermocline thickness after $\tau = 8$ h according to Eq. (17) in a complete absence of turbulence grows to only $t_{1^\circ\text{C}} = 0.38$ m whereas with $\alpha_{eff}/\alpha = 30$ it grows to $t_{1^\circ\text{C}} = 2$ m.

The importance of modeling α_{eff} to predict the thermocline evolution in water tanks is well known [13,14].

The flow field produced by square arrays of jets emerging from a perforated plate was studied experimentally by Villermaux and Hopfinger [24]. They defined the merging distance L as follows. Up to a downstream distance $x < L/2$, the jets remain coherent (i.e., the centerline jet velocity remains constant), the flow in the $z \times z \times L/2$ region delimited by four jets at its edges is essentially laminar and the instabilities of the jets due to the mild adverse pressure gradient are only weakly developed. But around $x \approx L/2$, the jets explode drastically, the centerline jet velocity drops abruptly, and the pressure has a corresponding small but abrupt S-shaped increase typical of a sudden expansion. In the downstream region between $L/2$ and $3L$ the vigorous turbulent mixing makes the mean velocity profile develop to essentially flat, and the pressure to reach the full far downstream recovery – calculated as

$$(P_\infty - P_0)/\rho w^2 = (4z^2/\pi\phi d^2) - 1 \quad (18)$$

with $z = 60$ mm and $d = 3, 5$ and 10 mm – is 1.56, 0.56 and 0.14 Pa respectively.

In [24], Villermaux and Hopfinger suggest that L/x scales as Re_{Vd}^{-1} , but the Re_{Vd} values they analyze only reach up to 3000. To the authors' knowledge, there is no extensive literature on this subject, especially with regard to perforated plates with very high solidity as in the present case. Therefore, the value of L has been determined based on the results of numerical simulations, as described at the beginning of Section 6.

In order to estimate the thermocline evolution downstream of the perforated plate, a two-region simplified model is adopted. In the region between $x = 0$ and $x = 3L$, it is assumed that the result of the laminar flow between $x = 0$ and $L/2$ and the vigorous turbulence mixing between $L/2$ and $3L$ is a thorough thermal mixing, effectively maintaining a uniform (but time-dependent) mean temperature $T_m(\tau)$. If T_0 denotes the temperature of the inflow through the plate orifices, the time evolution of $T_m(\tau)$ is obtained by solving the energy and mass balance equations. Assuming constant ρ and c , these are

$$3Lz^2\rho c \frac{dT_m}{d\tau} = (T_0 - T_L)\rho c V\phi\pi d^2/4 - (T_m - T_L)\rho c w z^2 + (q''_{x10} - q''_{x3L})z^2 \quad (19)$$

and

$$\rho V \phi \pi d^2 / 4 = \rho \omega z^2, \quad (20)$$

where $q''_x|_0 = (T_0 - T_m)h_0$ denotes the convective heat flux from the perforated plate (assumed at T_0) to the water, with heat transfer coefficient h_0 , and $q''_x|_{3L} = -(\alpha + \alpha_{\text{turb}})\rho c (\partial T/\partial x)_{3L^+}$ the heat flux between the fully mixed region and the downstream region, due to the nonzero temperature gradient on the downstream side ($3L^+$) of the interface at $3L$ between the two regions of the proposed simplified model. It is easy to verify that for any reasonable estimate of h_0 and $(\partial T/\partial x)_{3L^+}$ the two heat fluxes can be neglected here, because $|T_0 - T_m|_0 \ll |T_0 - T_L|\rho c w$ and $(\alpha + \alpha_{\text{turb}})\rho c |(\partial T/\partial x)_{3L^+}| \ll |T_m - T_L|\rho c w$. Therefore, considering the case of inflow at $T_0 = T_H$ into an initially uniform tank at T_L , the solution of Eq. (19) reduces to

$$\frac{T_m(\tau) - T_L}{T_H - T_L} = 1 - \exp\left(-\frac{\omega \tau}{3L}\right) \quad (21)$$

The region $x > 3L$ is instead modeled as a transient heat transfer problem governed by the energy balance equation

$$\frac{\partial T}{\partial \tau} + w \frac{\partial T}{\partial x} = \alpha \frac{\partial}{\partial x} \left[\left(1 + \frac{\alpha_{\text{turb}}}{\alpha}\right) \frac{\partial T}{\partial x} \right] \quad (22)$$

with boundary conditions

$$T(x = 3L, \tau) = T_m(\tau) \quad \partial T/\partial x|_H = 0 \quad (23)$$

Notice that in view of the very large diameter of the considered tank ($D/z = 325$) the effects of natural convection due to the thermal boundary layers which develop on the cold vertical cylindrical walls as well as the heat losses through these walls can be neglected on a relatively short time scale.

For numerical convenience the problem is cast in dimensionless form by defining the variables

$$\Theta = \frac{T(x - 3L, \tau) - T_L}{T_H - T_L} \quad \bar{\tau} = \frac{\omega \tau}{\alpha} \quad \bar{x} = \frac{(x - 3L)w}{\alpha} \quad \epsilon_{\text{eff}} = 1 + \frac{\alpha_{\text{turb}}}{\alpha} \quad (24)$$

$$\frac{\partial \Theta}{\partial \bar{\tau}} = \frac{\partial}{\partial \bar{x}} \left[-\Theta + \epsilon_{\text{eff}} \frac{\partial \Theta}{\partial \bar{x}} \right] \quad (25)$$

$$\Theta(0, \bar{\tau}) = 1 - \exp(-\bar{\tau}/3\bar{L}) \quad \bar{L} = Lw/\alpha \quad \partial \Theta/\partial \bar{x}|_{H, \bar{\tau}} = 0 \quad (26)$$

To close the problem, an expression for the turbulent thermal diffusivity α_{turb} as a function of the downstream coordinate x is needed.

In the region far downstream of the perforated plate ($x > 3L$), the mean (vertical) velocity is uniform (equal to zero when viewed from the moving frame $x = w\tau$) and the turbulence field is decaying. In fact, except for the natural convection flow generated by the cold walls, which is neglected here, there are no sources of turbulent kinetic energy, therefore, the turbulent thermal diffusivity can be taken [25] as

$$\alpha_{\text{turb}} = \frac{C_\mu}{Pr_{\text{turb}}} \frac{k^2}{\epsilon} \quad \text{with } \epsilon = -w \frac{dk}{dx} = \frac{k^2}{v Re_{\text{turb}}} \quad Re_{\text{turb}} = \frac{k^2}{v\epsilon} \quad (27)$$

where $C_\mu = 0.09$, $Pr_{\text{turb}} = 0.7$ is the turbulent Prandtl number, k the turbulence kinetic energy, ϵ the dissipation rate, and Re_{turb} the turbulence Reynolds number.

Equation (27) may be rewritten as

$$\frac{\alpha_{\text{turb}}}{\alpha} = \frac{C_\mu Pr}{Pr_{\text{turb}}} Re_{\text{turb}} \quad (28)$$

The variation of turbulence intensity with distance x downstream of a grid has been the subject of many experimental studies. According to George [26] a most comprehensive study covering a wide range of x/z is the one by Compte Bellot and Corrsin [27] where the data are correlated in terms of the grid pitch (z here), by a power law

$$\frac{k}{w^2 A} = \left[\frac{x - x_0}{z} \right]^{-n} \quad \frac{\epsilon z}{w^3 An} = \left[\frac{x - x_0}{z} \right]^{-n-1} \quad (29)$$

where x_0 is the virtual origin of the jet, and A a dimensionless constant which depends on the perforated plate geometry (z and d here) and the Reynolds number $Re_{wz} = wz/v$ (215 in the base case).

Combining Eqs. (27) and (29) yields:

$$\frac{\alpha_{\text{turb}}}{\alpha} = A \frac{C_\mu Pr Re_{wz}}{n Pr_{\text{turb}}} \left(\frac{L}{z}\right)^{1-n} \left[\left(\frac{\bar{x}}{\bar{L}}\right) - \left(\frac{x_0 - 3L}{L}\right) \right]^{1-n} \quad (30)$$

The values of A , n , and x_0 have been determined from the numerical simulations described at the beginning of Section 6.

6. Numerical results

For the determination of L/z , n , A and x_0 in Eq. (30), numerical simulations have been performed with the CFD software Ansys Fluent. The computational domain is the three-dimensional fluid region around the perforated plate. It extends for a length of $5d$ upstream of the perforated plate and $300d$ downstream of it in the direction of flow, being d the diameter of the circular holes drilled in the plate (3 mm, 5 mm and 10 mm). The cross section is a square of side $z/2$, where z is the center-to-center distance of the holes (pitch), equal to 60 mm, and it includes one quarter of a hole, the center located on one of its corners. Fig. 5 shows the section of the domain in correspondence of the upper surface of the plate, where water enters the tank, and the lateral view. The thickness t of the plate is 0.5 mm. On the surfaces delimiting the computational domain in the direction of the flow, symmetry boundary conditions have been imposed in order to simulate the mixing of the jets coming from the holes. On the square face upstream of the plate, velocity inlet boundary condition has been imposed, $w = 1.395$ mm/s and turbulence intensity 0.01%. On the opposite square face, outflow boundary condition has been set, which is assumed to be adequate given the distance from the plate. For the choice of the turbulence model, since no univocal indications were found in the literature, a preliminary series of simulations with $d = 3$ mm was performed using the six following turbulence models: standard $k - \epsilon$, renormalization group $k - \epsilon$, realizable $k - \epsilon$, standard $k - \omega$, shear stress transport $k - \omega$ and shear stress transport $k - \omega$ transitional flow. The results obtained in the first region of the jet, where the interaction between the various jets has not yet begun, were analyzed and compared with the data published by several authors for a single axial jet. This comparison demonstrated that neither standard $k - \epsilon$ nor standard $k - \omega$ models adequately solve the flow of an axial jet; on the other hand, shear stress transport $k - \omega$ and realizable $k - \epsilon$ models showed the best agreement in the trend along the axis of axial velocity, turbulence intensity and energy dissipation, and in the radial profiles of axial velocity and turbulence intensity in different axial positions. For this reason, for each hole diameter two simulations have been executed with two turbulence models: realizable $k - \epsilon$ (RKE) and shear stress transport $k - \omega$ (SSTKW).

The mesh is made of hexahedral and tetrahedral elements. Hexahedrons are used in the region close to the orifice (smallest-size elements) and from $20d$ downstream of the perforated plate (coarse elements). Tetrahedral elements make the connection between the two regions. The axial velocity decay along the hole axis was used to determine the mixing length $3L$, at which the axial velocity reaches the value w with a 1% tolerance. The values obtained with the two turbulence models are nearly coincident and are approximately $3L = 276$ mm for $d = 3$ mm, $3L = 270$ mm for $d = 5$ mm and $3L = 260$ mm for $d = 10$ mm. It is interesting to note that in all three cases the ratio $3L/z$ is about 4.5. In order to have an indication about the accuracy of the simulations, a comparison has been made of the value of $3L$ obtained in the case $d = 10$ mm with that of the merging distance from the correlation $L/z \sim Re_{Vd}^{-1}$ proposed in [24], since the Reynolds number in this case, equal to 2644, falls within the range investigated by the authors, up to 3000. After graphically deriving the coefficient of proportionality from that paper, $3L = 292$ mm is found, in good agreement with the value obtained from the simulation. On the other hand, poor agreement

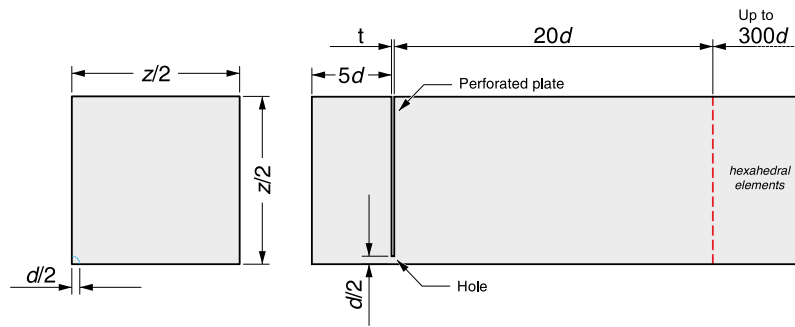


Fig. 5. Cross section (left) and lateral view (right) of the simulation domain.

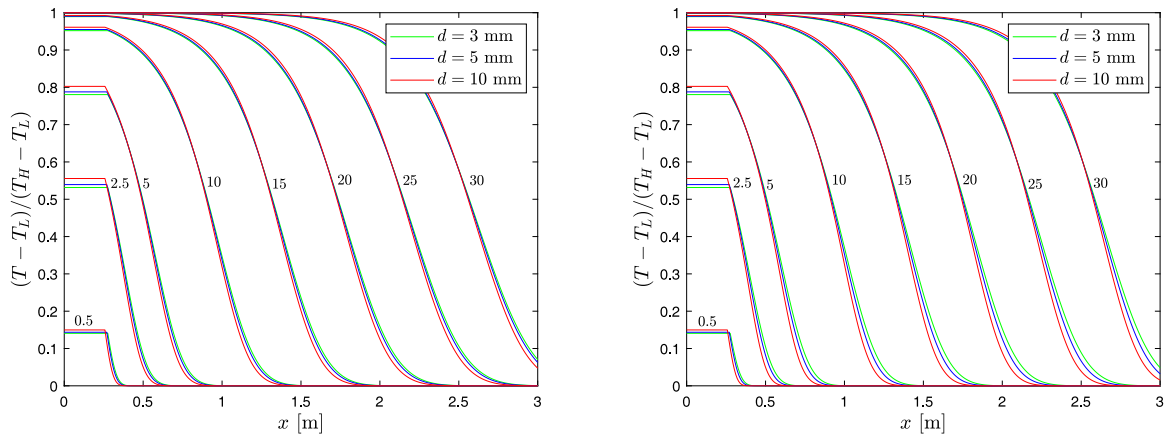


Fig. 6. Dimensionless temperature profiles at times $\tau = 0.5, 2.5, 5, 10, 15, 20, 25, 30$ min versus the distance x from the perforated plate during injection of water at T_H into the tank initially at uniform temperature T_L . $Q = 1500 \text{ m}^3/\text{h}$, $w = 1.395 \text{ mm/s}$. Parameters n , A and L obtained with SSTKW (left) and RKE (right) turbulence models.

Table 2
Values of n and A obtained with RKE and SSTKW turbulence models.

	SSTKW			RKE		
	n	A	R^2	n	A	R^2
$d = 3 \text{ mm}$	1.17	2.89	0.9905	1.52	6.39	0.9992
$d = 5 \text{ mm}$	1.14	2.41	0.9881	1.49	4.55	0.9992
$d = 10 \text{ mm}$	1.11	1.82	0.9900	1.45	2.81	0.9967

is found for the smaller diameters, which correspond to Reynolds numbers greater than 3000, further confirming the need for dedicated simulations in this case. Once the values of L were fixed, x_0 , n , and A in Eq. (30) have been determined by minimizing the root mean square deviation from the $\alpha_{\text{turb}}/\alpha$ curves along the x axis for $x \geq 3L$. For x_0 , the three values $2L$, $2.5L$, and $3L$ have been tested, and $2.5L$ has been chosen as it is the one yielding the largest coefficient of determination R^2 . The corresponding values of n , A , and R^2 for the two turbulence models are reported in Table 2.

The model Eqs. (24)–(26) and (30) have been implemented in MATLAB[®] using the pdepe solver which accepts partial differential equations with the structure of Eq. (25). Figs. 6 to 8 show the results of simulations of the initial tank charging transient, whereby injection of water at T_H begins at $\tau = 0$ when the water in the tank is at uniform temperature T_L . All simulations refer to the present design parameters, $w = 1.395 \text{ mm/s}$ and $z = 60 \text{ mm}$, with three orifice diameters, $d = 3, 5$, and 10 mm . The temperature of the water in the tank ranges between $T_L = 60^\circ\text{C}$ (cold water) and $T_H = 98^\circ\text{C}$ (hot water). The properties of water are assumed at the average temperature of 80°C and their values can be found in Section 2.

Fig. 6 shows the dimensionless temperature profiles plotted versus the downstream distance x from the perforated plate at the eight time instants $\tau = 0.5, 2.5, 5, 10, 15, 20, 25, 30$ min. The modeling

assumption of uniform temperature $T_m(\tau)$ over the merging distance L is clearly visible and obviously a drastic idealization. The profiles show no significant difference between the three investigated diameters, the target temperature of $\theta = 0.98$ being reached in about 15 min in all cases.

Fig. 7 shows that, when viewed from an observer that moves downstream at the mean flow velocity w , the same profiles (as well as those at all later times of the tank charging process) change in time: in particular, the thermocline thickness increases considerably, and this effect is especially evident with SSTKW turbulence model. Indeed, Fig. 8 shows that values of $\alpha_{\text{turb}}/\alpha$ predicted with RKE model are initially higher, but more rapidly decaying, than with SSTKW. This behavior results in different thermocline thicknesses $t_{\delta T}$ obtained with the two models, as shown in Fig. 9 for $\delta T = 2^\circ\text{C}$ and $\delta T = 5^\circ\text{C}$.

The role of turbulence, through the effective thermal diffusivity, is particularly important in the jet mixing region immediately downstream of the plate. Figs. 10 and 11 show the temperature profiles and the thermocline growth during the charging process for four values of $(\alpha_{\text{turb}}/\alpha)|_{x=3L}$ with the same parameters n , A and L (i.e., with the same decay law) obtained from simulations with SSTKW and RKE turbulence models.

It is noteworthy that the proposed model does not consider the effects of buoyancy during the initial phase of injection. When hot water is injected through the orifices into the initially cold layer immediately downstream of the perforated plate, buoyancy will favor the jets breakup and merging, the jet penetration will be reduced, and the fully mixed region will be shorter. This is beneficial in that the smaller mixing region will take less time to heat up, resulting in a thinner thermocline. In other words, the effect of neglecting buoyancy is an overestimation of the thermocline thickness, as confirmed by the experimental evidence reported in next section.

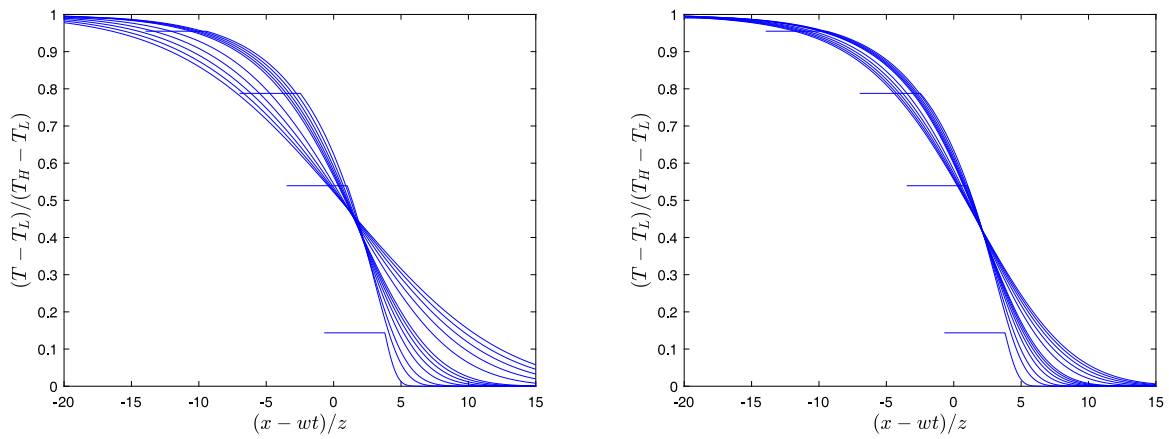


Fig. 7. Dimensionless temperature profiles plotted versus the shifted distance $x - wt$ nondimensionalized by the jet pitch z for $d = 5$ mm perforation. Parameters n , A and L obtained with SSTKW (left) and RKE (right) turbulence models. In addition to the first eight profiles of Fig. 6 here also those at times $\tau = 1, 1.5, 2, 2.5, 3$ h are shown.

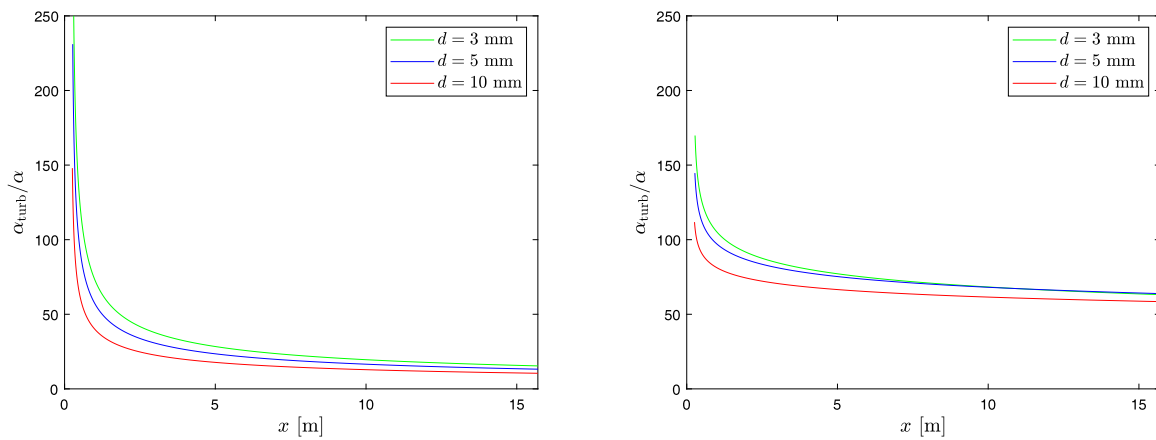


Fig. 8. Turbulent thermal diffusivity ratio α_{turb}/α versus the distance x from the perforated plate, for the profiles of Fig. 7. Parameters n , A and L obtained with SSTKW (left) and RKE (right) turbulence models.

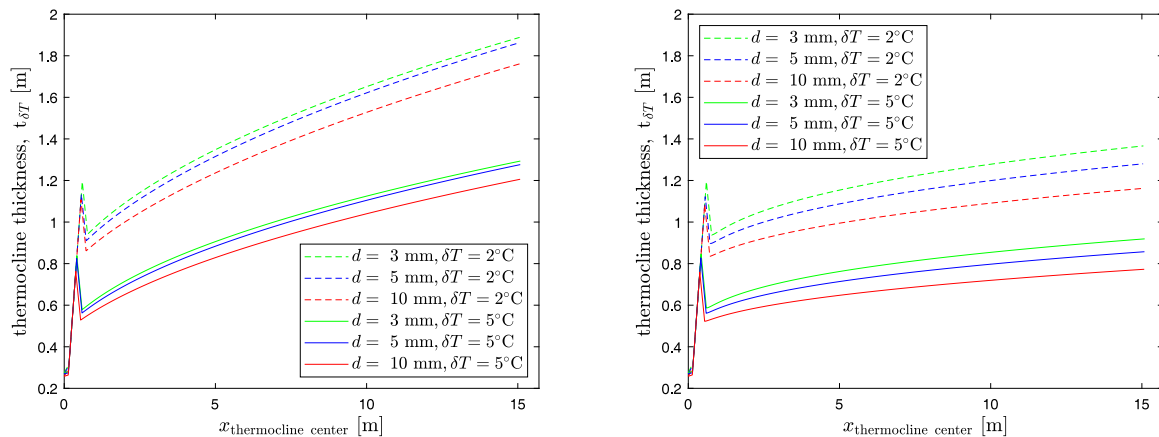


Fig. 9. Thermocline thicknesses t_{2c} and t_{5c} versus the position of thermocline center, for the profiles of Fig. 7. Parameters n , A and L obtained with SSTKW (left) and RKE (right) turbulence models. The sharp peaks correspond to the temperature of the fully mixed layer reaching $T_H - \delta T$, when $t_{\delta T}$ suddenly drops by about $3L$.

7. Experimental validation

The proposed design is currently being adopted in several storage tanks of the district heating network of A2A Calore & Servizi utility company, operating in Northern Italy. The first storage tank of the kind is the system described in Section 2, with a diameter of 19.5 m and an actual storage height of 17.5 to 18.5 m (stored volume: 5226–5525 m³).

The installed perforated plates feature 5 mm diameter orifices and 60 mm uniform pitch. The storage tank, located in Brescia, Italy, has been completed in the summer of 2020 (Fig. 12).

During operation, vertical temperatures in the TES are measured by Pt100 resistance temperature detectors (RTD) installed in thermowells at different elevations (10 equally spaced-apart sensors between 1.8 m and 15.3 m, two pairs of sensors at 0.75/0.95 m and 16.5/16.7 m,

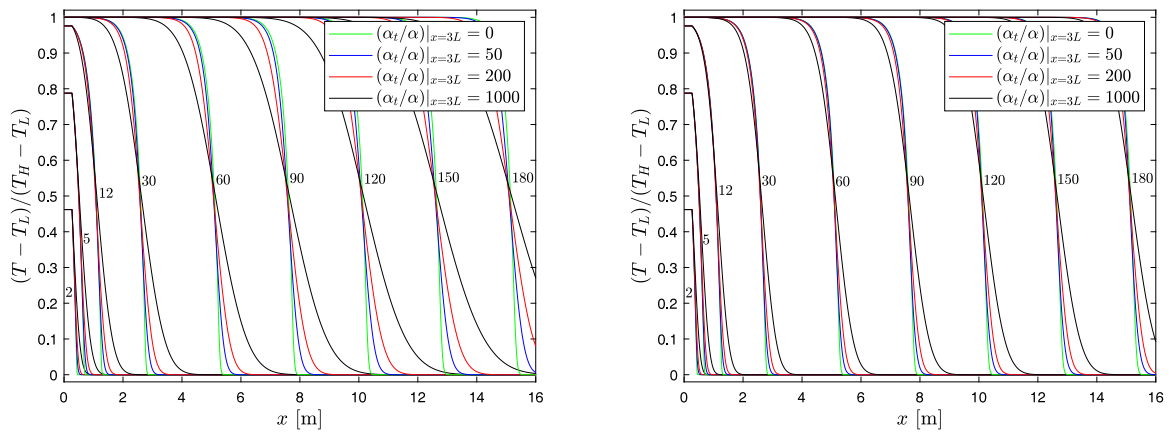


Fig. 10. Effect of the value of $(\alpha_t/\alpha)|_{x=3L}$ on the temperature profiles after 2, 5, 12, 30, 60, 90, 120, 180 min. $Q = 1500 \text{ m}^3/\text{h}$, $w = 1.395 \text{ mm/s}$, $d = 5 \text{ mm}$. Parameters n , A and L obtained with SSTKW (left) and RKE (right) turbulence models.

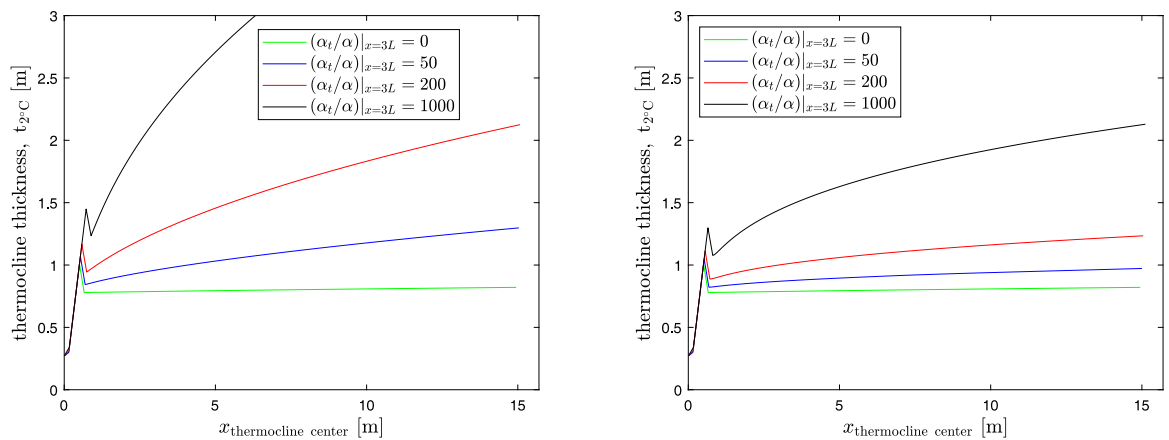


Fig. 11. Thermocline thickness versus the position of center, for the profiles of Fig. 10. Parameters n , A and L obtained with SSTKW (left) and RKE (right) turbulence models.

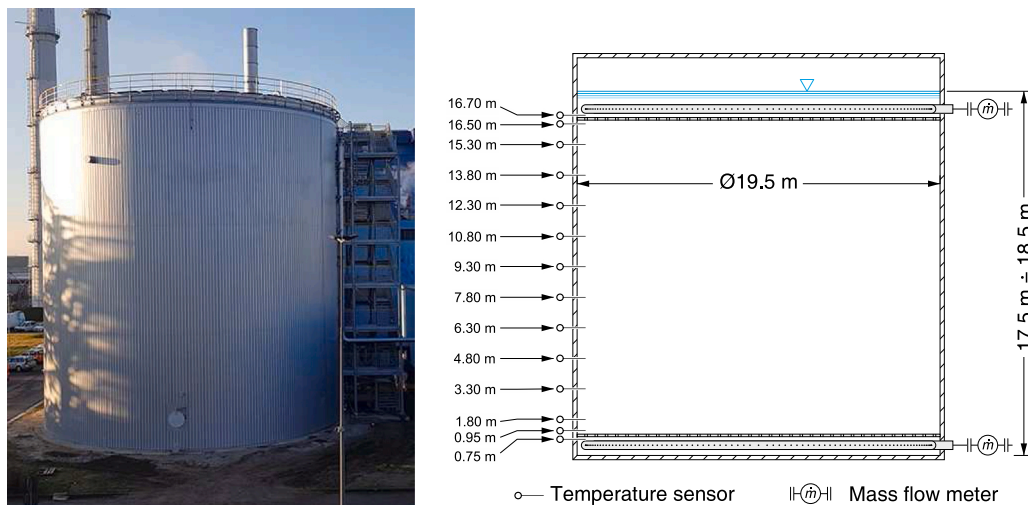


Fig. 12. Storage tank featuring toroidal manifolds and perforated plates, installed in Brescia in 2020.

upstream and downstream of the rectifying plates). The thermowell tips, thus the RTDs, are immersed in the hot water at a distance of 0.6 m from the tank wall. Flow rates are also measured at the inlet and outlet connections of the tank with the network. Details on the measurement instruments can be found in Table 3. The uncertainty of temperature measurements has been estimated by retrieving the maximum deviations due to accuracy class, the influence of ambient

temperature, maximum thermoelectric voltage, and signal transmitter from the technical datasheet of the instrument, and applying the law of propagation of error. Uncertainty of flow rate measurements has been derived from maximum error indicated on the flow meter datasheet.

The analysis is based on preliminary measurements collected in the 2020–2021 heating season and provided as a weighted average on 300 s. For an RTD data set, it is possible to estimate the displacement of

Table 3

Characteristics of the measurement instruments installed on the analyzed TES (m.v.: measured value).

Quantity	Sensor type	Range	Maximum error
Temperature	Pt100, 3 wire	0 ... 150°C	$\pm(0.278\% \text{ m.v.} + 0.20 \text{ K})$
Flow rate	Ultrasonic	0 ... 2000 m ³ /h	$\pm(0.3\% \text{ m.v.} + 2 \text{ mm/s})$

Table 4

Details of selected experimental charging transient.

Quantity	Value
Start time	11:25 PM, 2021/01/14
End time	04:45 AM, 2021/01/15
Average water velocity (min/max)	0.65 mm/s (−0.3%/+0.4%)
Minimum temperature	65.74°C
Maximum temperature	96.74°C

the water mass in the measurement interval $\delta\tau$ as $\delta x = 4Q_{\text{meas}}\delta\tau/(\pi D^2)$, where Q_{meas} is the average between the flow rates measured at the endpoints of the interval. The cumulative displacement of the water mass at a certain time τ is the sum of all the δx values between the initial measurement and τ .

To evaluate the prediction capability of the analytical model, a portion of a charging transient with approximately constant water velocity has been isolated (see details in Table 4). Fig. 13 shows the evolution of the thermocline during the transient. The temperatures measured by RTDs at different heights are plotted as a function of a cumulative displacement Δx , calculated as:

$$\Delta x(\tau) = \Delta x_{\text{period}} - \left[\sum_{q=0}^{\tau} \delta x(q) + (h_j - h_{\text{up}}) \right] \quad (31)$$

where Δx_{period} is the total estimated displacement of the water mass at the end of the given charge period, and h_j and h_{up} are the elevations of the j th RTD and of a reference position, i.e. the upper plate. With this formulation, the curves for different temperature measurement points overlap and can be compared directly. The shaded area in Fig. 13 represents the expanded uncertainty of temperature measurements, estimated as described above, and the expanded uncertainty of displacement, estimated with the Monte-Carlo method applied to Eq. (31) considering only the contributions of flow rate measurements, with 10^6 trials. For both quantities, the uncertainty is presented with 95% confidence, resulting in maximum values of 0.91 K and 0.009 m, respectively.

It can be observed that the thermocline remains quite stable throughout the transient, thus its thickness was evaluated on the average curve, considering $\delta T = 5^\circ\text{C}$ from the highest and lowest temperatures recorded during the transient. The resulting estimated thickness $t_{\delta T}$ is 0.55 m. It is worth noting the difference with respect to the plots in Figs. 7 and 9, where the shape and thickness of the thermocline rapidly change in time. In this regard, the parameters found with the RKE turbulence model seem to provide a closer representation of the experimental evidence than those obtained with the SSTKW model.

In the light of these considerations, Fig. 14 shows the comparison between experimental measurements and analytical results with A , n and L derived from the RKE model (see Table 2), where both sets of data are converted to non-dimensional values using the same T_H and T_L reported in Table 4.

The quality of the agreement is extremely sensitive to the value of n , which modifies the slope of the curves, while it is hardly influenced by changes in A . Therefore, an optimization has been made to choose the n that provides the best agreement with measured data. In detail, the procedure selects the value that minimizes the root mean square error (RMSE) in the slope of the simulated curves with respect to the experimental ones. The analysis has been limited to the central portion of the thermocline, that is, where the non-dimensional temperatures fall between 0.3 and 0.7, and considering a range of possible n values

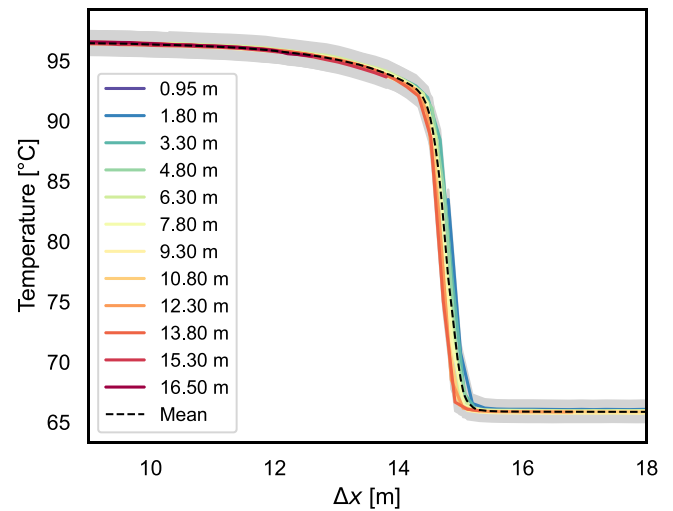


Fig. 13. Measured thermocline evolution during the selected charging transient. Shaded area: expanded uncertainty of measured temperatures and calculated displacements with 95% confidence.

between 1.5 and 4. It has been found that RMSE stabilizes after $n = 2.5$, with a minimum reached at $n = 3.3$, that is, at higher values than those obtained from CFD simulations. It is worth noting that the estimation of n exponent for the decay of homogeneous turbulence has been the subject of many fundamental studies (see for example [25–28]), where values of 10/7, 6/5, and 1 are given based on different assumed levels of self-preservation, except in the final, viscosity-dominated decay region where it approximates 5/2. Indeed, the values of n obtained from the simulations (see Table 2) are all in this range, with slightly higher values for the RKE turbulence model. However, values comparable with the experimentally-derived n are also reported and discussed in the literature. In 2007, for the first time, faster turbulence decay was observed downstream of fractal grids [29]. This anomalous behavior was later confirmed by some authors still downstream of fractal grids [30,31], while other authors observed non-classical decay in turbulence generated by multi-scale grids [32]: in particular, in the latter paper, the authors highlighted how a faster decay is observed in the region immediately downstream of the grid, whereas the classical decay characterizes the far-downstream region. In 2012, it was stated in [33] that in the region immediately downstream of fractal grids (but of regular grids as well) turbulence is highly inhomogeneous, and for this reason the dimensionless normalized dissipation coefficient is not constant. The behavior of the normalized dissipation coefficient has also been recently studied in [34] with similar results. The interesting review by Vassilicos [35] clearly illustrated the process that allowed to recognize and accept the faster decay of turbulence downstream of grids since the turbulence generated by a grid is different from the homogeneous turbulence in a box. In 2018, Meldi and Sagaut attributed the high decay exponents to the shape of the turbulence spectrum [36]. As a further confirmation, one can refer to the paper by Hearst and Lavoie [37], in which the authors experimentally analyzed the decay of turbulence downstream of a fractal grid, and proposed the decay exponents 2.79 for $3.5 \leq x/z \leq 20.0$, and 1.39 for $20.3 \leq x/z \leq 48.5$. The authors also determined the virtual origin x_0 based on the agreement of the curves obtained for different values of x_0/z with the experimental data: the proposed values in their case were -8.0 and $+7.0$ for the closest and the subsequent region, respectively.

Based on these considerations, the exponent $n > 2.5$ here estimated from experimental data seems reasonable.

Fig. 15 shows the evolution of the profiles predicted by the analytical model when $n = 3.3$ is used: it can be observed that the curves now fall onto an almost universal profile, indicating that the thermocline

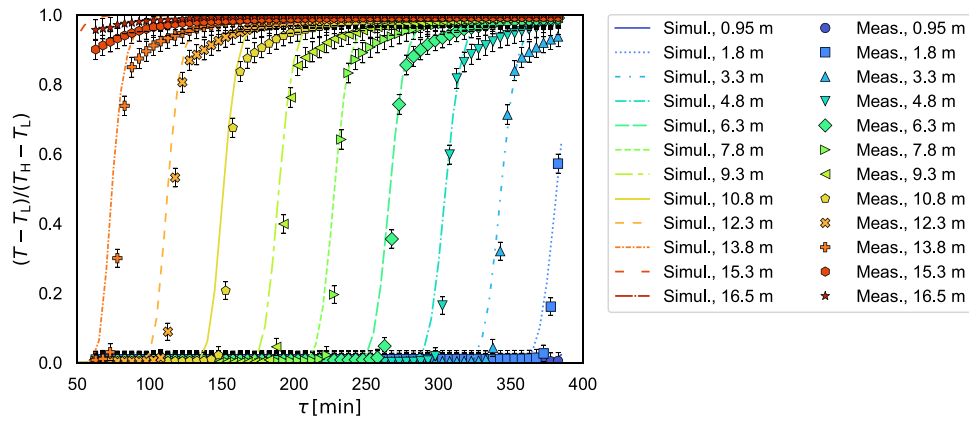


Fig. 14. Comparison between simulations ($d = 5$ mm; $n = 1.49$; $A = 4.55$, see Table 2, and $x_0 = 2.5L = 0.225$ m from simulations with the RKE model) and experimental measurements for the selected charging transient (error bars: 95% confidence interval).

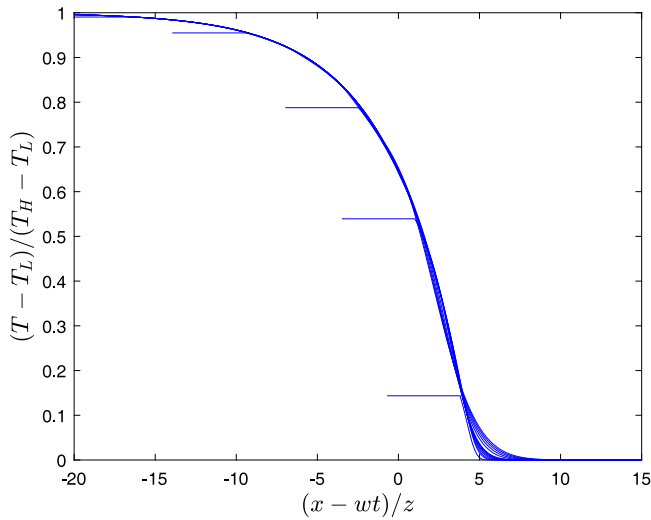


Fig. 15. Dimensionless temperature profiles at times $\tau = 0.5, 2.5, 5, 10, 15, 20, 25, 30, 60, 90, 120, 150, 180$ min, plotted versus the shifted distance $x - wt$ nondimensionalized by the jet pitch z for $d = 5$ mm perforation. $n = 3.3$; parameters A and L obtained with RKE turbulence model.

shape and thickness are established in the first few minutes of the charging process, in the region of jet breakup and merging, strong convective mixing and high turbulent diffusivity. This description better applies to the experimental evidence than the situation depicted in the right graph in Fig. 7, where the thermocline shape changes considerably over time, and the parameters are the same as in Fig. 15 except for $n = 1.49$.

Fig. 16 shows the results of the comparison between model predictions and temperature measurements obtained setting n to the optimized value of 3.3, and A and x_0 to the values obtained from simulations with the RKE model ($A = 4.55$, see Table 2, and $x_0 = 2.5L = 0.225$ m).

The agreement is good except in the non-dimensional temperature region between 0.9 and 1, corresponding to the transition between the thermocline and the hot fluid. The reason for this discrepancy lies in the different way the storage tank is actually operated with respect to the assumptions of the analytical model. Indeed, the model assumes that the water flowing through the perforated plate during the charging

process is at the highest temperature. However, in real conditions, the system is almost completely discharged, so that hot water enters the tank above the perforated plate and mixes with cold water before reaching the flow-rectifying device. As a result, the perforated plate consolidates the mixed layer and generates a smoother thermocline than predicted. That being said, the transient-average thermocline thickness according to the analytical model is 0.51 m, which is only 8% below the experimental evidence.

The list of parameters to be fed as input to the 1D model described in Section 6, and their values to obtain the curves in Figs. 14 and 16 are summarized in Table 5.

8. Conclusions

The present study proposes an innovative inlet/outlet distribution system for large water thermal energy storages to be installed in district heating networks. The top and bottom distributors are characterized by a perforated inlet/outlet pipe and a flow-rectifying perforated plate. Key design parameters such as the orifice diameter and the perforation pitch are chosen based on analytical considerations and empirical correlations for the effects of decaying turbulence intensity on the effective thermal diffusivity downstream of a perforated plate.

A simplified one-dimensional model to simulate the time evolution of the temperature distribution and the thermocline thickness in the storage section of the tank is proposed and solved numerically to help evaluate the relative effects of the various fluid mechanics and heat transfer details that are simultaneously in play. The large size and the wall insulation of the tank allow neglecting the two-dimensional features of the flow due to the thermal boundary layers which develop on the cold tank walls and focusing on the one-dimensional features of turbulent mixing and diffusivity.

Nevertheless, the analysis highlights the relatively complex fluid dynamics and heat transfer phenomenology in play, and calls for further modeling and experimental efforts. Due to the lack of literature models that could provide characteristic turbulence parameters for the proposed inlet perforated plate, they have been estimated by CFD simulations and subsequently verified in the light of experimental data. It was found that the choice of the turbulence model has an impact on the results, and that RKE model seems to provide a closer representation of the problem. Experimental measurements showed that the decay of turbulence is faster than originally expected according to both the analytical model and the CFD simulations: as a result, the thermocline is established immediately downstream of the perforated plate, and remains practically constant along time. The discrepancy between CFD-calibrated analytical predictions and experimental evidence are likely

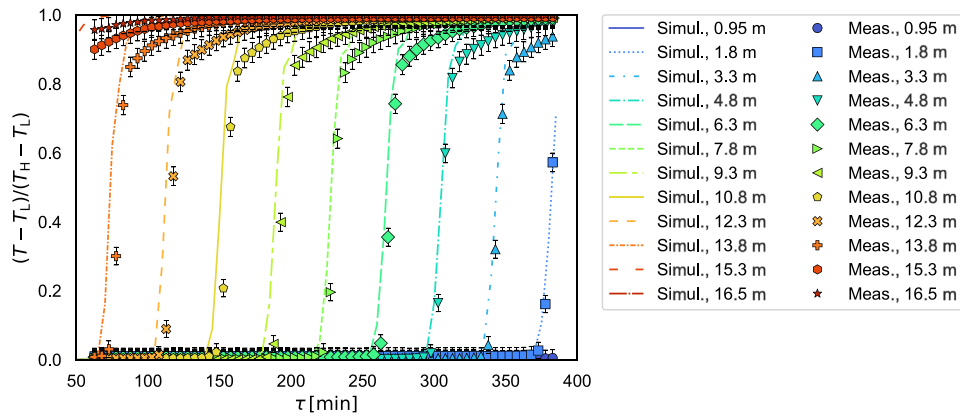


Fig. 16. Comparison between simulations ($d = 5$ mm; optimized $n = 3.3$; $A = 4.55$, see Table 2, and $x_0 = 2.5L = 0.225$ m from simulations with the RKE model) and experimental measurements for the selected charging transient (error bars: 95% confidence interval).

Table 5

Input data required by 1D model for the comparison with experimental data (Figs. 14 and 16).

Parameter	Symbol	Unit	Value
Water density (80°C)	ρ	kg/m ³	975
Water specific heat (80°C)	c_p	J/(kg K)	4197
Inside diameter of the tank	D	m	19.5
Water free surface height	H_{eff}	m	18
Upper plate elevation	h_{upper_plate}	m	16.6
Lower plate elevation	h_{lower_plate}	m	0.85
Minimum temperature	T_{min}	°C	60
Maximum temperature	T_{max}	°C	100
Thermocline threshold	δT	K	5
Plate perforation pitch	z	m	0.06
Plate orifice diameter	d	m	0.005
Water mass velocity	w	m/s	6.51×10^{-4}
Discharge coefficient	ϕ	-	0.62
Prandtl number	Pr	-	2.38
Turbulent Prandtl number	Pr_{turb}	-	0.7
Water thermal conductivity (80°C)	λ	W/(m K)	0.67
Water dynamic viscosity (80°C)	μ	Pa s	3.8×10^{-4}
Merging distance over plate perforation pitch	$3L/z$	-	4.5
Virtual origin of the jet	x_0	m	0.225
Geometrical dimensionless constant	A	-	4.55
Turbulence decay exponent from RKE simulations (Fig. 14)	n	-	1.49
Turbulence decay exponent from experiments (Fig. 16)	n	-	3.3

due to two main aspects: first, the model does not consider buoyancy, which has a positive effect in that it reduces the height of the mixing region, and second, the turbulence models used in the CFD simulations to estimate n , A and L parameters assume homogeneous turbulence even in the zone immediately downstream of the perforated plate, where, on the other hand, the presence of a faster decay is documented by both recent literature studies and experimental measurements. This behavior also implies that, if a mixed layer is created in the upper portion of the tank, it is consolidated by the passage through the flow-rectifying device. Therefore, planning adequate charge/discharge cycles is a possible strategy to further improve the storage performances of the system.

Declaration of competing interest

One or more of the authors of this paper have disclosed potential or pertinent conflicts of interest, which may include receipt of payment, either direct or indirect, institutional support, or association with an entity in the biomedical field which may be perceived to have potential conflict of interest with this work. For full disclosure statements refer to <https://doi.org/10.1016/j.apenergy.2022.119436>. Gian Paolo Beretta reports financial support was provided by Lombardy Region, Italy. Mariagrazia Pilotelli reports financial support was provided by Lombardy Region, Italy. Benedetta Grassi reports financial support was provided by Lombardy Region, Italy.

Acknowledgments

This study was sponsored in part by the Regione Lombardia, Italy project “Smart Grid Pilot: Banco EnerGETICO” (CUP E89I17000410009, Asse I, POR FESR 2014–2020). We thank ingg. Daniele Pasinelli, Luca Bertagna, Alessandro Gnatta, and Marco Riello of A2A Calore & Servizi for several useful discussions, and ing. Lorenzo Zaniboni of A2A Ambiente for the opportunity to use Ansys Fluent software.

Appendix A. Maldistribution in injection and suction modes of a perforated manifold

This Appendix presents a general simplified model and solution of the mass and momentum balance equations for a perforated manifold of length L_T immersed in a constant static pressure pool under the assumption that pressure drops due to the axial flow inside the manifold are negligible with respect to the dissipative effects due to the flow through the orifices.

During the injection mode, the section at $s = 0$ is the manifold inlet, where the inlet axial flow speed is $U_{0,inj}$ and the static pressure $P_{0,inj}$ is higher than the pool pressure P_a downstream of the orifices.

During the suction mode, the section at $s = 0$ is the manifold outlet, where the outlet axial flow speed is $U_{0,suc}$ and the static pressure $P_{0,suc}$ is lower than the pool pressure P_a upstream of the orifices.

For model simplicity, the assumptions are that the volume flow rate Q_s is in the axial direction, the mean axial velocity U_s , the centerline pressure P_s , and the orifice pitch z_s are continuous function of s , so that the mass conservation equation along the perforated pipe may be written as

$$V_s = -\frac{4z_s R_{TCS}^2}{\pi \phi d_T^2} \frac{dQ_s}{ds} = -\frac{4z_s R_{TCS}^2}{\phi d_T^2} \frac{dU_s}{ds} \quad (A.1)$$

where R_{TCS} is the manifold inner cross-sectional radius, d_T the orifice diameter (assumed equal for all orifices), V_s the mean velocity at the orifice *vena contracta*, and ϕ its discharge coefficient, that is, its area contraction factor with respect to the actual orifice area, which following [16] and references therein, is assumed equal to 0.62 for both suction and injection. The direction of V_s is inward during suction and outward during injection.

The pressure drop across the orifices is assumed to obey the relations

$$P_s - P_a = (1 - K_{inj}) \frac{1}{2} \rho V_s^2 \quad \text{injection mode} \quad (A.2)$$

$$P_a - P_s = (1 - K_{suc}) \frac{1}{2} \rho V_s^2 \quad \text{suction mode} \quad (A.3)$$

where K_{inj} and K_{suc} are static pressure regain coefficients, that bear the usually small effects of the Reynolds number and the pipe wall thickness. For simplicity, these coefficients are assumed to be also sufficient to bear the effects of the pressure drops inside the manifold due to friction, flow bending at injection to feed the orifice jet and cross mixing at suction of the jet and the axial stream. Therefore, the momentum balance is the Bernoulli equation applied to the axial streamline between s and 0,

$$P_s + \frac{1}{2} \rho U_s^2 = P_{0,inj} + \frac{1}{2} \rho U_{0,inj}^2 \quad \text{injection mode} \quad (A.4)$$

$$P_s + \frac{1}{2} \rho U_s^2 = P_{0,suc} + \frac{1}{2} \rho U_{0,suc}^2 \quad \text{suction mode} \quad (A.5)$$

Therefore, the dependence of U_s is regulated by the differential equation obtained by eliminating V_s and P_s from Eqs. (A.1), (A.2), and (A.4), for the injection mode

$$\frac{4z_s R_{TCS}^2}{\phi d_T^2 U_{0,inj}} \sqrt{1 - K_{inj}} \frac{dU_s}{ds} = - \left[\frac{P_{0,inj} - P_a}{\frac{1}{2} \rho U_{0,inj}^2} + 1 - \frac{U_s^2}{U_{0,inj}^2} \right]^{1/2} \quad (A.6)$$

with boundary conditions $U_s(0) = U_{0,inj}$ and $U_s(L_T) = 0$, and from Eqs. (A.1), (A.3), and (A.5), for the suction mode

$$\frac{4z_s R_{TCS}^2}{\phi d_T^2 U_{0,suc}} \sqrt{1 - K_{suc}} \frac{dU_s}{ds} = - \left[\frac{P_a - P_{0,suc}}{\frac{1}{2} \rho U_{0,suc}^2} - 1 + \frac{U_s^2}{U_{0,suc}^2} \right]^{1/2} \quad (A.7)$$

with boundary conditions $U_s(0) = U_{0,suc}$ and $U_s(L_T) = 0$.

These equations can be rewritten in compact form as

$$-a_{inj} \frac{du_{inj}}{\sqrt{1 - u_{inj}^2}} = \frac{d\bar{s}}{\bar{z}(\bar{s})} \quad \text{injection mode} \quad (A.8)$$

$$-a_{suc} \frac{du_{suc}}{\sqrt{1 + u_{suc}^2}} = \frac{d\bar{s}}{\bar{z}(\bar{s})} \quad \text{suction mode} \quad (A.9)$$

in terms of the following dimensionless parameters and variables

$$a_{inj} = \frac{4R_{TCS}^2 \sqrt{1 - K_{inj}}}{\phi d_T^2} \quad a_{suc} = \frac{4R_{TCS}^2 \sqrt{1 - K_{suc}}}{\phi d_T^2} \quad (A.10)$$

$$p_{inj} = \frac{P_{0,inj} - P_a}{\frac{1}{2} \rho U_{0,inj}^2} \quad p_{suc} = \frac{P_a - P_{0,suc}}{\frac{1}{2} \rho U_{0,suc}^2} \quad (A.11)$$

$$u_{inj} = \frac{U_s}{U_{0,inj} \sqrt{p_{inj} + 1}} \quad u_{suc} = \frac{U_s}{U_{0,suc} \sqrt{p_{suc} - 1}} \quad (A.12)$$

$$\bar{s} = s/L_T \quad \bar{z} = z_s/L_T \quad (A.13)$$

Integrated from $s = 0$ to $s = L_T$ they yield the conditions

$$a_{inj} \arcsin \left(\frac{1}{\sqrt{p_{inj} + 1}} \right) = a_{suc} \operatorname{arcsinh} \left(\frac{1}{\sqrt{p_{suc} - 1}} \right) = \int_0^1 \frac{d\bar{s}}{\bar{z}(\bar{s})} \quad (A.14)$$

which relate the dimensionless static pressure differences p_{inj} and p_{suc} to the chosen orifice pitch distribution $\bar{z}(\bar{s})$.

The general solutions are

$$u_{inj} = \sin \left(\frac{1}{a_{inj}} \int_{\bar{s}}^1 \frac{d\bar{s}}{\bar{z}(\bar{s})} \right) \quad (A.15)$$

$$u_{suc} = \sinh \left(\frac{1}{a_{suc}} \int_{\bar{s}}^1 \frac{d\bar{s}}{\bar{z}(\bar{s})} \right) \quad (A.16)$$

and clearly exhibit the general relation between the dimensionless flow velocity distributions in the manifold during injection and suction

$$a_{inj} \arcsin(u_{inj}) = a_{suc} \operatorname{arcsinh}(u_{suc}) = \int_{\bar{s}}^1 \frac{d\bar{s}}{\bar{z}(\bar{s})} \quad (A.17)$$

These can be inserted into Eq. (A.1), rewritten in terms of the dimensionless variable, to obtain the distributions of the *vena contracta* dimensionless velocities $v_{inj} = V_s/U_{0,inj}$ and $v_{suc} = V_s/U_{0,suc}$,

$$v_{inj} = -\frac{\sqrt{p_{inj} + 1}}{\sqrt{1 - K_{inj}}} a_{inj} \bar{z} \frac{du_{inj}}{d\bar{s}} = \frac{\sqrt{p_{inj} + 1}}{\sqrt{1 - K_{inj}}} \cos \left(\frac{1}{a_{inj}} \int_{\bar{s}}^1 \frac{d\bar{s}}{\bar{z}(\bar{s})} \right) \quad (A.18)$$

$$v_{suc} = -\frac{\sqrt{p_{suc} - 1}}{\sqrt{1 - K_{suc}}} a_{suc} \bar{z} \frac{du_{suc}}{d\bar{s}} = \frac{\sqrt{p_{suc} - 1}}{\sqrt{1 - K_{suc}}} \cosh \left(\frac{1}{a_{suc}} \int_{\bar{s}}^1 \frac{d\bar{s}}{\bar{z}(\bar{s})} \right) \quad (A.19)$$

No maldistribution in injection mode

Now suppose that a design priority is to have no maldistribution during the injection mode. This requires that dU_s/ds be constant, or, in dimensionless variables, that $du_{inj}/d\bar{s} = -1/\sqrt{p_{inj} + 1}$ so that $u_{inj} = (1 - \bar{s})/\sqrt{p_{inj} + 1}$. Inserting these conditions in Eq. (A.8) yields the required orifice pitch distribution

$$\bar{z}(\bar{s}) = a_{inj}^{-1} \sqrt{p_{inj} + (2 - \bar{s})\bar{s}} \quad (A.20)$$

which coincides with Eq. (4) of the main text. Once this pitch distribution has been chosen, the integral in Eqs. (A.14), (A.15) and (A.16) is set, $\int_{\bar{s}}^1 \bar{z}(\bar{s})^{-1} d\bar{s} = a_{inj} \arcsin[(1 - \bar{s})/\sqrt{p_{inj} + 1}]$ and so are the operating values of p_{inj} and p_{suc} .

With the orifice pitch distribution given by Eq. (A.20), Eq. (A.15) reduces to $u_{inj} = (1 - \bar{s})/\sqrt{p_{inj} + 1}$ showing that during the injection mode the manifold features no maldistribution regardless of the imposed pressure difference $P_{0,inj} - P_a$. However, the pitch distribution fixes the value of p_{inj} once and for all and, therefore, Eq. (A.11) yields the inlet flow speed into the manifold, $U_{0,inj} = \sqrt{(P_{0,inj} - P_a)/\frac{1}{2} \rho p_{inj}}$.

For the suction mode, Eq. (A.16) yields

$$u_{suc} = \sinh \left\{ (a_{inj}/a_{suc}) \arcsin[(1 - \bar{s})/\sqrt{p_{inj} + 1}] \right\} \quad (A.21)$$

showing that the flow will be maldistributed because $du_{suc}/d\bar{s}$ is not constant. However, for sufficiently large p_{inj} this solution is approximated by

$$u_{suc} \approx (a_{inj}/a_{suc}) \times [(1 - \bar{s})/\sqrt{p_{inj} + 1}] \{ 1 + [1 + (a_{inj}/a_{suc})^2](1 - \bar{s})^2/6(p_{inj} + 1) \} \quad (A.22)$$

so that

$$du_{suc}/d\bar{s} \approx -(a_{inj}/a_{suc}) \times (1/\sqrt{p_{inj} + 1}) \{ 1 + [1 + (a_{inj}/a_{suc})^2](1 - \bar{s})^2/2(p_{inj} + 1) \}$$

(A.23)

showing that $du_{\text{suc}}/d\bar{s}$ during suction is not constant but has a quadratic dependence on \bar{s} of the order of $(p_{\text{inj}} + 1)^{-1}$.

A simple measure of the degree of maldistribution can be defined by

$$\eta_{\text{inj}} = \frac{-du_{\text{inj}}/d\bar{s}|_{\bar{s}=1} + du_{\text{inj}}/d\bar{s}|_{\bar{s}=0}}{-du_{\text{inj}}/d\bar{s}|_{\bar{s}=1}} \quad \eta_{\text{suc}} = \frac{-du_{\text{suc}}/d\bar{s}|_{\bar{s}=1} + du_{\text{suc}}/d\bar{s}|_{\bar{s}=0}}{-du_{\text{suc}}/d\bar{s}|_{\bar{s}=1}} \quad (\text{A.24})$$

Therefore, for $p_{\text{inj}} \gg 1$ the nonuniform pitch distribution according to Eq. (A.20) yields $\eta_{\text{inj}} = 0$ and $\eta_{\text{suc}} = [1 + (a_{\text{inj}}/a_{\text{suc}})^2]/2(p_{\text{inj}} + 1)$. For example, $\eta_{\text{suc}} = 10\%$ for $a_{\text{inj}}/a_{\text{suc}} = 1$ and $p_{\text{inj}} = 9$.

Maldistribution in injection and suction modes for uniform orifice pitch

Another obvious design option could be to privilege the construction simplicity of a uniform orifice pitch, $\bar{z} = \text{const}$, accepting to have some degree of maldistribution during both injection and suction. In this case, the choice of \bar{z} determines p_{inj} and p_{suc} through Eq. (A.14),

$$p_{\text{inj}} = \cot^2(1/a_{\text{inj}}\bar{z}) \quad p_{\text{suc}} = \coth^2(1/a_{\text{suc}}\bar{z}) \quad (\text{A.25})$$

Equations (A.15) and (A.16) yield

$$u_{\text{inj}} = \sin \left[(1 - \bar{s}) \arcsin \left(\frac{1}{\sqrt{p_{\text{inj}} + 1}} \right) \right] \quad (\text{A.26})$$

$$u_{\text{suc}} = \sinh \left[(1 - \bar{s}) \operatorname{arcsinh} \left(\frac{1}{\sqrt{p_{\text{suc}} - 1}} \right) \right] \quad (\text{A.27})$$

and the degrees of maldistribution turn out to be

$$\eta_{\text{inj}} = 1 - \cos(1/a_{\text{inj}}\bar{z}) = 1 - (1 + p_{\text{inj}}^{-1})^{-1/2} \quad (\text{A.28})$$

$$\eta_{\text{suc}} = 1 - \cosh(1/a_{\text{suc}}\bar{z}) = 1 - (1 - p_{\text{suc}}^{-1})^{-1/2} \quad (\text{A.29})$$

For example, with $a_{\text{inj}}/a_{\text{suc}} = 1$ and $p_{\text{inj}} = 9$ it yields $p_{\text{suc}} = 10.33$, $\eta_{\text{inj}} = 5.13\%$ and $\eta_{\text{suc}} = -5.22\%$. As $p_{\text{inj}}, p_{\text{suc}} \gg 1$ the degrees of maldistribution are well approximated by $\eta_{\text{inj}} = 1/2p_{\text{inj}}$ and $\eta_{\text{suc}} = -1/2p_{\text{suc}}$.

Appendix B. Shape of the free surface over the upper perforated plate

The Bernoulli equation applied to a radial streamline lying on the free surface of the water layer on top of the upper perforated plate is

$$P_{\text{atm}} + \rho g h_r + \frac{1}{2} \rho U_r^2 = P_{\text{atm}} + \rho g h_R + \frac{1}{2} \rho U_R^2 \quad (\text{B.1})$$

Inserting Eq. (12) it becomes

$$h_r + \frac{w^2 r^2}{8g h_r^2} = h_R + \frac{w^2 R^2}{8g h_R^2} = h_c \quad (\text{B.2})$$

This can be rewritten as a cubic equation

$$(1 - y_r^2) y_r = \frac{w^2 r^2}{8g h_c^3} \quad \text{in the unknown} \quad y_r = \frac{h_c - h_r}{h_c} = \frac{w^2 r^2}{8g h_c h_r^2} \quad (\text{B.3})$$

which can be solved to find the shape h_r of the free surface.

In this case,

$$\frac{w^2 r^2}{8g h_c^3} \ll 1 \quad (\text{B.4})$$

therefore the solution of Eq. (B.3) is a parabolic profile

$$y_r \approx \frac{w^2 r^2}{8g h_c^3} \ll 1 \quad \text{i.e.} \quad h_r = (1 - y_r) h_c \approx h_c \quad (\text{B.5})$$

which nonetheless is essentially flat.

References

- [1] Novo AV, Bayon JR, Castro-Fresno D, Rodriguez-Hernandez J. Review of seasonal heat storage in large basins: Water tanks and gravel-water pits. *Appl Energy* 2010;87(2):390–7. <http://dx.doi.org/10.1016/j.apenergy.2009.06.033>.
- [2] Andrews D, Krook-Riekkola A, Tzimas E, Serpa J, Carlsson J, Pardo-Garcia N, et al. Background report on EU-27 district heating and cooling potentials, barriers, best practice and measures of promotion. 2012. <http://dx.doi.org/10.2790/47209>.
- [3] Guelpa E, Marincioni L, Verda V. Towards 4th generation district heating: Prediction of building thermal load for optimal management. *Energy* 2019;171:510–22. <http://dx.doi.org/10.1016/j.energy.2019.01.056>.
- [4] Verda V, Colella F. Primary energy savings through thermal storage in district heating networks. *Energy* 2011;36(7):4278–86. <http://dx.doi.org/10.1016/j.energy.2011.04.015>.
- [5] Herwig A, Umbreit L, Rühling K. Measurement-based modelling of large atmospheric heat storage tanks. In: *Energy procedia*. vol. 149, 2018, p. 179–88. <http://dx.doi.org/10.1016/j.egypro.2018.08.182>, ISSN: 1876-6102.
- [6] Romanchenko D, Odenberger M, Göransson L, Johnsson F. Impact of electricity price fluctuations on the operation of district heating systems: A case study of district heating in göteborg, Sweden. *Appl Energy* 2017;204:16–30. <http://dx.doi.org/10.1016/j.apenergy.2017.06.092>.
- [7] Deng N, He G, Gao Y, Yang B, Zhao J, He S, et al. Comparative analysis of optimal operation strategies for district heating and cooling system based on design and actual load. *Appl Energy* 2017;205:577–88. <http://dx.doi.org/10.1016/j.apenergy.2017.07.104>.
- [8] Chung JD, Cho SH, Tae CS, Yoo H. The effect of diffuser configuration on thermal stratification in a rectangular storage tank. *Renew Energy* 2008;33(10):2236–45. <http://dx.doi.org/10.1016/j.renene.2007.12.013>.
- [9] Altuntop N, Arslan M, Ozceyhan V, Kanoglu M. Effect of obstacles on thermal stratification in hot water storage tanks. *Appl Therm Eng* 2005;25(14–15):2285–98. <http://dx.doi.org/10.1016/j.applthermaleng.2004.12.013>.
- [10] Zachár A, Farkas I, Szlivka F. Numerical analyses of the impact of plates for thermal stratification inside a storage tank with upper and lower inlet flows. *Sol Energy* 2003;74(4):287–302. [http://dx.doi.org/10.1016/S0038-092X\(03\)00188-9](http://dx.doi.org/10.1016/S0038-092X(03)00188-9).
- [11] Lavan Z, Thompson J. Experimental study of thermally stratified hot water storage tanks. *Sol Energy* 1977;19(5):519–24. [http://dx.doi.org/10.1016/0038-092X\(77\)90108-6](http://dx.doi.org/10.1016/0038-092X(77)90108-6).
- [12] Zurigat YH, Ghajar AJ. Heat transfer and stratification in sensible heat storage systems. In: *Thermal energy storage: Systems and applications*. New York: Wiley; 2002.
- [13] Zurigat YH, Ghajar AJ, Moretti PM. Stratified thermal storage tank inlet mixing characterization. *Appl Energy* 1988;30(2):99–111. [http://dx.doi.org/10.1016/0306-2619\(88\)90007-4](http://dx.doi.org/10.1016/0306-2619(88)90007-4).
- [14] Zurigat YH, Liche PR, Ghajar AJ. Influence of inlet geometry on mixing in thermocline thermal energy storage. *Int J Heat Mass Transfer* 1991;34(1):115–25. [http://dx.doi.org/10.1016/0017-9310\(91\)90179-1](http://dx.doi.org/10.1016/0017-9310(91)90179-1).
- [15] Kocijel L, Mrzljak V, Glažar V. Numerical analysis of geometrical and process parameters influence on temperature stratification in a large volumetric heat storage tank. *Energy* 2020;194. <http://dx.doi.org/10.1016/j.energy.2019.116878>.
- [16] Bailey BJ. Fluid flow in perforated pipes. *J Mech Eng Sci* 1975;17(6):338–47. http://dx.doi.org/10.1243/JMES_JOUR_1975_017_048_02.
- [17] Taliyan SS, Roy DP, Grover RB, Singh M, Govindarajan S. An experimental study of the discharge coefficient of pipe perforations. *Exp Fluids* 1995;19(5):348–52. <http://dx.doi.org/10.1007/BF00203420>.
- [18] Kolodzie Jr PA, Van Winkle M. Discharge coefficients through perforated plates. *AIChE J* 1957;3(3):305–12. <http://dx.doi.org/10.1002/aic.690030304>.
- [19] Smith Jr PL, Van Winkle M. Discharge coefficients through perforated plates at reynolds numbers of 400 to 3000. *AIChE J* 1958;4(3):266–8. <http://dx.doi.org/10.1002/aic.690040306>.
- [20] Şahin B. Pressure losses in an isolated perforated plate and jets emerging from the perforated plate. *Int J Mech Sci* 1989;31(1):51–61. [http://dx.doi.org/10.1016/0020-7403\(89\)90118-5](http://dx.doi.org/10.1016/0020-7403(89)90118-5).
- [21] Malavasi S, Messa G, Fratino U, Pagano A. On the pressure losses through perforated plates. *Flow Meas Instrum* 2012;28:57–66. <http://dx.doi.org/10.1016/j.flowmeasinst.2012.07.006>.
- [22] Tseng C-C, Li C-J. Numerical investigation of the inertial loss coefficient and the porous media model for the flow through the perforated sieve tray. *Chem Eng Res Des* 2016;106:126–40. <http://dx.doi.org/10.1016/j.cherd.2015.12.017>.
- [23] Carslaw HS, Jaeger JC. *Conduction of heat in solids*. 2nd ed. London, UK: Oxford University Press; 1959, (par. 2.15, pp. 87–88).
- [24] Villiermaux E, Hopfinger EJ. Periodically arranged co-flowing jets. *J Fluid Mech* 1994;263:63–92. <http://dx.doi.org/10.1017/S0022112094004039>.
- [25] Pope SB. *Grid turbulence*. In: *Turbulent flows*. London: Cambridge University Press; 2000, p. 158–61.
- [26] George WK. The decay of homogeneous isotropic turbulence. *Phys Fluids A* 1992;4(7):1492–509. <http://dx.doi.org/10.1063/1.858423>.

- [27] Comte-Bellot G, Corrsin S. The use of a contraction to improve the isotropy of grid-generated turbulence. *J Fluid Mech* 1966;25(4):657–82. <http://dx.doi.org/10.1017/S0022112066000338>.
- [28] Liu R, Ting DS-K, David Checkel M. Constant Reynolds number turbulence downstream of an orificed perforated plate. *Exp Therm Fluid Sci* 2007;31(8):897–908. <http://dx.doi.org/10.1016/j.exthermfluidsci.2006.09.007>.
- [29] Seoud ER, Vassilicos CJ. Dissipation and decay of fractal-generated turbulence. *Phys Fluids* 2007;19(10). <http://dx.doi.org/10.1063/1.2795211>.
- [30] Discetti S, Ziskin IB, Astarita T, Adrian RJ, Prestridge KP. PIV measurements of anisotropy and inhomogeneity in decaying fractal generated turbulence. *Fluid Dyn Res* 2013;45(6). <http://dx.doi.org/10.1088/0169-5983/45/6/061401>.
- [31] Gomes-Fernandes R, Ganapathisubramani B, Vassilicos JC. Particle image velocimetry study of fractal-generated turbulence. *J Fluid Mech* 2012;711:306–36. <http://dx.doi.org/10.1017/jfm.2012.394>.
- [32] Krogstad P-Å, Davidson PA. Freely decaying, homogeneous turbulence generated by multi-scale grids. *J Fluid Mech* 2011;680:417–34. <http://dx.doi.org/10.1017/jfm.2011.169>.
- [33] Valente PC, Vassilicos JC. Universal dissipation scaling for nonequilibrium turbulence. *Phys Rev Lett* 2012;108(21). <http://dx.doi.org/10.1103/PhysRevLett.108.214503>.
- [34] Djenidi L, Lefeuvre N, Kamruzzaman M, Antonia RA. On the normalized dissipation parameter C_ϵ in decaying turbulence. *J Fluid Mech* 2017;817:61–79. <http://dx.doi.org/10.1017/jfm.2017.110>.
- [35] Vassilicos JC. Dissipation in turbulent flows. *Annu Rev Fluid Mech* 2015;47:95–114. <http://dx.doi.org/10.1146/annurev-fluid-010814-014637>.
- [36] Meldi M, Sagaut P. Investigation of anomalous very fast decay regimes in homogeneous isotropic turbulence. *J Turbul* 2018;19(5):390–413. <http://dx.doi.org/10.1080/14685248.2018.1450506>.
- [37] Hearst RJ, Lavoie P. Decay of turbulence generated by a square-fractal-element grid. *J Fluid Mech* 2014;741:567–84. <http://dx.doi.org/10.1017/jfm.2013.684>.